

# JGR Earth Surface

## RESEARCH ARTICLE

10.1029/2020JF005848

### Key Points:

- Bedrock weathering and water storage patterns are similar across a sequence of ridges and valleys
- Discrete fracturing and discoloration extend deeper into the hillslope relative to pyrite and organic carbon oxidation
- The relief of weathering fronts above local channels scales with hillslope length

### Supporting Information:

Supporting Information may be found in the online version of this article.

### Correspondence to:

M. A. Pedrazas,  
michellepedrazas@utexas.edu

### Citation:

Pedrazas, M. A., Hahm, W. J., Huang, M.-H., Dralle, D., Nelson, M. D., Breunig, R. E., et al. (2021). The relationship between topography, bedrock weathering, and water storage across a sequence of ridges and valleys. *Journal of Geophysical Research: Earth Surface*, 126, e2020JF005848. <https://doi.org/10.1029/2020JF005848>

Received 21 AUG 2020  
Accepted 23 FEB 2021

## The Relationship Between Topography, Bedrock Weathering, and Water Storage Across a Sequence of Ridges and Valleys

Michelle A. Pedrazas<sup>1</sup> , W. Jesse Hahm<sup>2</sup> , Mong-Han Huang<sup>3</sup> , David Dralle<sup>4</sup> , Mariel D. Nelson<sup>1</sup>, Rachel E. Breunig<sup>1</sup> , Kristen E. Fauria<sup>5</sup> , Alexander B. Bryk<sup>6</sup>, William E. Dietrich<sup>6</sup>, and Daniella M. Rempe<sup>1</sup>

<sup>1</sup>Department of Geosciences, Jackson School of Geosciences, The University of Texas at Austin, Austin, TX, USA,

<sup>2</sup>Department of Geography, Simon Fraser University, Burnaby, BC, Canada, <sup>3</sup>Department of Geology, University of Maryland, College Park, MD, USA, <sup>4</sup>Pacific Southwest Research Station, United States Forest Service, Albany, CA, USA,

<sup>5</sup>Department of Earth and Environmental Sciences, Vanderbilt University, Nashville, TN, USA, <sup>6</sup>Department of Earth and Planetary Science, University of California, Berkeley, CA, USA

**Abstract** Bedrock weathering regulates nutrient mobilization, water storage, and soil production. Relative to the mobile soil layer, little is known about the relationship between topography and bedrock weathering. Here, we identify a common pattern of weathering and water storage across a sequence of three ridges and valleys in the sedimentary Great Valley Sequence in Northern California that share a tectonic and climate history. Deep drilling, downhole logging, and characterization of chemistry and porosity reveal two weathering fronts. The shallower front is ~7 m deep at the ridge of all three hillslopes, and marks the extent of pervasive fracturing and oxidation of pyrite and organic carbon. A deeper weathering front marks the extent of open fractures and discoloration. This front is 11 m deep under two ridges of similar ridge-valley spacing, but 17.5 m deep under a ridge with nearly twice the ridge-valley spacing. Hence, at ridge tops, the fraction of the hillslope relief that is weathered scales with hillslope length. In all three hillslopes, below this second weathering front, closed fractures and unweathered bedrock extend about one-half the hilltop elevation above the adjacent channels. Neutron probe surveys reveal that seasonally dynamic moisture is stored to approximately the same depth as the shallow weathering front. Under the channels that bound our study hillslopes, the two weathering fronts coincide and occur within centimeters of the ground surface. Our findings provide evidence for feedbacks between erosion and weathering in mountainous landscapes that result in systematic subsurface structuring and water routing.

**Plain Language Summary** The patterns of bedrock weathering concealed beneath the surface have important implications for the water cycle. In many upland landscapes, sequences of ridges and valleys result from river incision into bedrock, which organizes the landscape into hillslopes separated by channels. While surface topography of these landscapes is easily visible, the structure of weathered bedrock beneath the surface and its relationship to overlying topography are unknown. In this study, we observed systematic patterns of weathering and water storage under three hillslopes that make up a repeating ridge-valley sequence formed in sedimentary bedrock. Across the study area, weathering is thickest under ridges and thins downslope toward adjacent valleys, where fresh bedrock lies almost directly below channels. Interestingly, the depth of extensive weathering and seasonal water storage at the ridges was comparable across all three hillslopes, while open fractures and discoloration persist to a deeper depth under the longer hillslope. These observations provide a basis for scaling point measurements of weathering to the landscape scale, which is a much-needed tool for models of earth surface processes.

## 1. Introduction

The surface topography of many landscapes is organized into repeating ridges and valleys (Hack & Goodlett, 1960; Hovius, 1996; Perron et al., 2008, 2009; Shaler, 1899; Talling et al., 1997), indicative of a commonality in process resulting in a similarity in hillslope form. Is the structure of the subsurface similarly organized, exhibiting a common or repeated form? The study of soil production and transport has revealed

© 2021. The Authors.

This is an open access article under the terms of the Creative Commons Attribution-NonCommercial License, which permits use, distribution and reproduction in any medium, provided the original work is properly cited and is not used for commercial purposes.

relationships between topography and soil thickness, such that the physically mobile soil layer varies systematically with hillslope curvature (Heimsath et al., 1997). The pattern of weathering of the underlying bedrock, which influences water and sediment transport, may also be related to topography in some way. However, because this structure is hidden below ground, our observations are limited to sporadic roadcuts, quarries, drilling, and geophysical imaging. In comparison to the readily observable soil and land surface, we have a poor understanding of the pattern of weathered bedrock at landscape scales.

The limited field data that exist have motivated a number of process-based conceptual models that couple the evolution of the land surface and the bedrock weathering front. In considering the time evolution of these mechanisms, it is useful to think in terms of “unit hillslopes,” that span individual channel-todivide-to-channel landscape units. Channel incision at the base of a hillslope defines the boundary condition for soil transport and landsliding, creating a hillslope form that reflects the relevant transport processes. Given constant tectonic uplift, erosion can progressively lead to steady-state topography (e.g., Armstrong, 1980; Gilbert, 1909; Heimsath et al., 1997; Hirano, 1975; Roering et al., 2001; Willett et al., 2001). In this context, one can consider the mechanisms that link the evolution of surface topography to processes that alter bedrock by weathering. Observational studies of weathering profiles across different rock types, tectonic regimes, and climates (e.g., Brantley, Holleran, et al., 2013; Hahm et al., 2019; St. Clair et al., 2015) have motivated model frameworks, which incorporate specific weathering mechanisms. One approach for treating the relationship between topography and the depth of weathering is parallel to established soil production functions whereby the rate of weathering front propagation is an inverse function of the thickness of weathering (Booth et al., 2013; Hilley et al., 2010). Another approach is to consider the influence of hillslope topographic orientation and convexity on fracture penetration as driven by frost cracking or regional stress fields (Anderson, Anderson, & Tucker, 2013; Slim et al., 2015; St. Clair et al., 2015). Other approaches are centered around the way in which water penetrates and drains from hillslopes. For example, the position of the water table, and thus the maximum penetration of reactive, meteoric gases, has been linked to the maximum depth of weathering (Goodfellow et al., 2011; Wan et al., 2019). Rempe and Dietrich (2014) consider the movement of water within the unweathered bedrock. They propose that the pace of the lowering of the elevation of chemically equilibrated groundwater in a hillslope may be driven by channel incision that induces lateral drainage. Other studies emphasize lateral water fluxes within the weathered bedrock, whereby climate plays a role through the rate of groundwater recharge and delivery of meteoric waters to the base of the weathering front (Anderson, Rajaram, & Anderson, 2019; Brantley, Lebedeva, et al., 2017; Harman & Cosans, 2019). Taken together, these proposed mechanisms support the notion that the spatial pattern of weathered bedrock can evolve in tandem with the land surface. Furthermore, this suggests that the depth of weathering may be inferred from topography alone in some cases.

The spatial pattern of bedrock weathering depth has important consequences across a wide range of Earth surface processes. Mounting evidence suggests that weathered bedrock plays a critical role in routing water and/or nutrients through hillslopes (e.g., Canadell et al., 1996; Hasenmueller et al., 2017; Jackson et al., 1999; Nie et al., 2011; Sternberg et al., 1996; Witty et al., 2003). Rooting in bedrock is common, and water stored in weathered bedrock can be a critical water supply to plants, especially in drought years (Arkley, 1981; Hubbert et al., 2001; Jackson et al., 1999; Lewis & Burg, 1964; Rempe & Dietrich, 2018; Rose et al., 2003; Scholl, 1976; Schwinnig, 2010; Zwieniecki & Newton, 1996). Drainage from weathered bedrock generates streamflow, determines streamflow chemistry, and in many cases sustains baseflow during dry periods (e.g., Lovill et al., 2018; Montgomery et al., 1997; Onda, Komatsu, et al., 2001; Onda, Tsujimura, & Tabuchi, 2004; Salve et al., 2012; Uchida et al., 2002). The extent to which weathered bedrock is altered also plays a significant role in landscape evolution. Because weathered bedrock determines how water is routed through hillslopes, it also impacts subsurface pore pressures, which regulate shallow landslide triggering and earthflow velocities (Bennett et al., 2016; Booth et al., 2013; Montgomery & Dietrich, 1994). The extent to which bedrock is altered before becoming mobile soil is important to predict the size distribution and competence of sediment delivered to channels, which impacts channel incision (Sklar et al., 2017). In applied engineering, delimiting the extent of deep weathering is vital to any project requiring solid bedrock for foundations or the knowledge of water movement in the subsurface (Ruxton & Berry, 1959; Schoenberger et al., 1995).

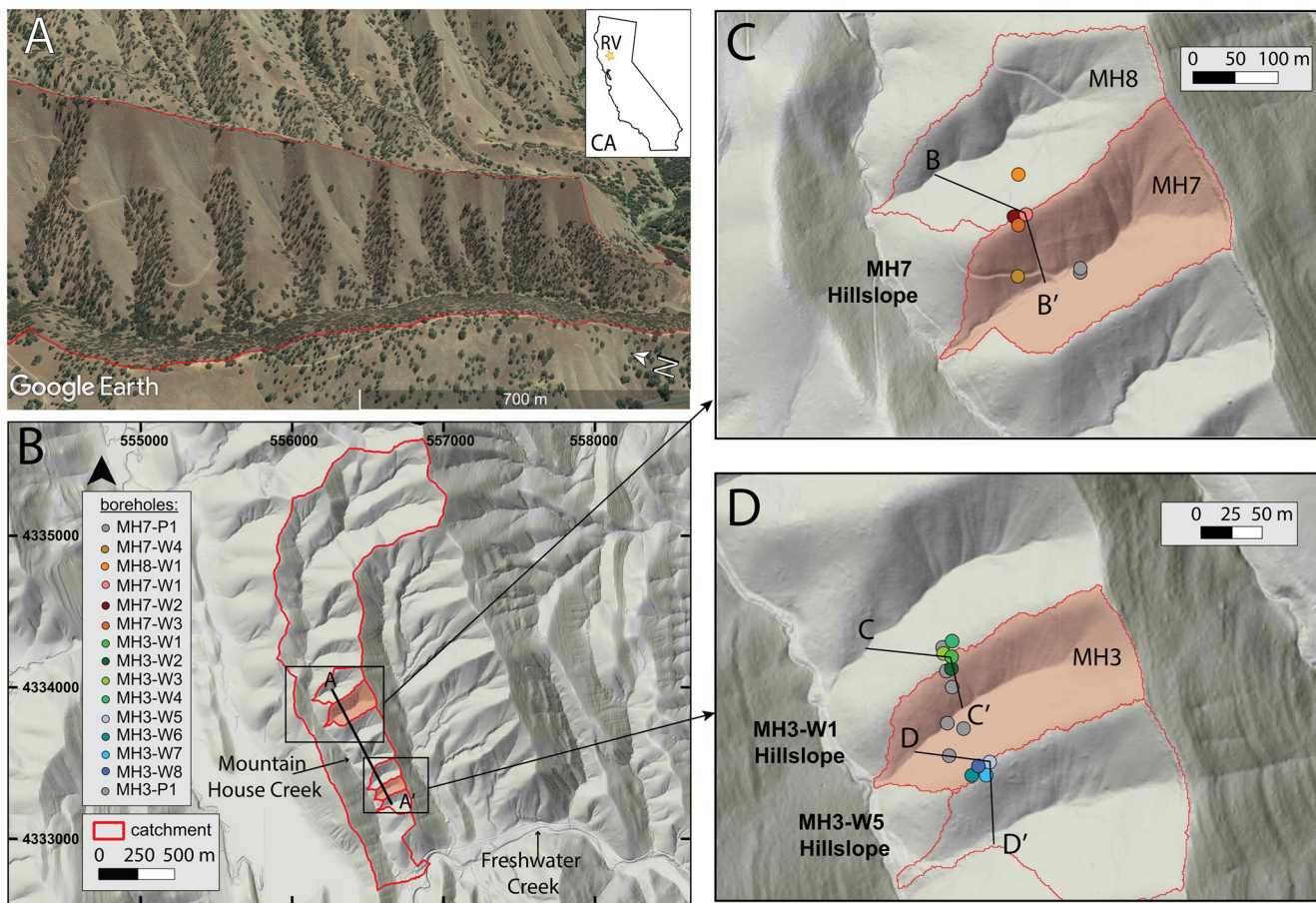


**Figure 1.** (a) is a Google Earth image of the study site (with terrain height-scaled 2x), where the red outlines delineate the Mountain House catchment and subcatchments. (b–d) are hillshade maps of the study site, where (c and d) are hillshade maps zoomed in to the MH7 and MH3 hillslopes (respectively) and include borehole locations and cross-sections lines, which are used to illustrate hillslope profiles in Figures 2 and 8.

In spite of the importance of bedrock weathering, its spatial pattern at landscape scales remains largely *terra incognita*. Improving our capacity to predict and map the subsurface across hillslopes at regional scales has been identified as a key research frontier for earth system models (Fan et al., 2019; Pelletier et al., 2016). Studies of weathering profiles in one- or two-dimensions have identified key characteristics and guided new hypotheses and models, but it has not yet been established that weathering profiles within a given landscape should have some systematic structure or relationship with topography. Furthermore, the relationship between depth of weathering and depth of dynamic water storage (in the unsaturated and saturated zones) is unclear. In this paper, we investigate the weathering profile structure under hillslopes in a highly structured ridge-valley sequence through deep drilling. We exploit three hillslopes with common underlying lithology, climate and tectonic history, which share hillslope form but have distinct ridge-valley spacing. We hypothesize that topography and subsurface weathering processes respond to similar boundary conditions over similar timescales such that a systematically structured weathering profile emerges and repeats across individual hillslopes.

## 2. Site Description

The topography of our study area is strongly controlled by regional geology: topographic ridges, meter-scale topographic perturbations influenced by underlying lithologic bedding, and drainages tend to lie parallel or perpendicular to the regional strike of dipping sedimentary beds (Dohrenwend, 1974). The study watershed ( $39.1474^\circ$ ,  $-122.3447^\circ$ ; Figure 1b) is on private ranchland (Rancho Venada), 16 km west of Williams, California. The watershed is unnamed on the USGS topographic quadrangle of the area (Manor

Slough). Indigenous residents of the local area include members of the Kletsel Dehe Wintun Nation. We have dubbed the study watershed Mountain House after the historic settlement at the watershed mouth. Mountain House Creek is seasonally ephemeral, and drains to the south where it joins the east-flowing Freshwater Creek, which cuts through ridges on the eastern edge of the Northern California Coast Ranges before meeting the Central Valley (creeks labeled in Figure 1b). The drainages that flow to the west within the Mountain House (MH) catchment are named in ascending order moving northward from the catchment mouth (MH0, MH1, etc.). Study hillslopes are located within the MH subcatchments (Figures 1c, 1d, and S1).

## 2.1. Geologic and Tectonic Setting

The site is underlain by steeply dipping ( $50\text{--}60^\circ$  to the east) marine sedimentary beds of the Great Valley Sequence, which strike north-north-west. The homoclinal beds lie to the east of the Stony Creek fault zone and extend east under the Sacramento Valley (Rich, 1971). The highest resolution geologic map of the area, by Rich (1971) at a scale of 1:48,000, describes rocks under the study hillslopes as predominantly thinly bedded and laminated Cretaceous mudstones to siltstones, containing Albian and Cenomanian-aged macrofossils. Laterally extensive sandstone lenses are also common, and consist primarily of quartz, feldspar, and rock fragments (Rich, 1971). The beds are interpreted to result from a mixture of fine-grained hemipelagic sedimentation interspersed with episodic coarse-grained sedimentation associated with turbidity currents (Rich, 1971). A variety of models have been put forward to describe the structure and timing of the post-Cretaceous uplift and tilting of the western Great Valley Sequence that underlies our field area (see e.g., Constenius et al., 2000). Based on structural relationships, fossils, and seismic surveys, these works generally indicate that deformation (uplift) of the Great Valley Sequence was greatest between the mid-Miocene to late-Pleistocene (Ernst, 1970; Hackel, 1966), primarily along blind thrust faults (e.g., Unruh & Moores, 1992).

## 2.2. Topographic Description

The Mountain House catchment is  $1.58 \text{ km}^2$  and ranges from 94 to 581 m above sea level, with a mean elevation of 293 m. A series of hillslopes with successively larger topographic relief are aligned from south to north in the lower half of the Mountain House catchment. The site, like the surrounding eastern edge of the Northern California Coast Ranges underlain by the Great Valley Sequence, is highly organized into ridge-valley topography at a variety of scales. Major ridges and drainages trend parallel to the strike of the bedding. Field surveys of bedrock exposure in Freshwater Creek confirm the lithologic descriptions of Rich (1971). Bedrock exposures in channel beds tend to occur where recent landslides and/or debris flows promoted local scour. The bedrock also manifests itself across both the exposed-bedrock and soil-mantled portions of the hillslopes as north-north-west trending lineations. The eastern boundary of the Mountain House catchment is a thick unit of sandstone that appears to “hold up” the ridge. The sandstone ridgeline consists of an exposed bedrock escarpment of 3–4 m that sheds large boulders. On both the eastward-facing slopes bordering the west side of Mountain House Creek and the east-facing slopes to the east of the eastern watershed boundary there are subtle topographically convergent zones, but no substantially incised valleys. Although at a coarse scale it appears that these eastward-facing slopes are dip slopes (i.e., defined by an individual, laterally extensive bed), the bedding dips more steeply than the ground surface, and upon closer examination a series of lineations defining the intersection of bedding with the ground surface is visible in spite of the continuous presence of a soil mantle on both westward and eastward-facing slopes (Figure 1). Cattle graze during part of the year, and many portions of the landscape are heavily terraced along contour by their walking, with approximately half-meter tread-riser step sequences.

Some of the west-flowing drainages within the lower portion of the Mountain House catchment terminate in mixed debris and alluvial fans, visible in the field and in the Light Detection and Ranging (LiDAR) map of Figure 1b (data collected by the National Center for Airborne Laser Mapping). In general, however, there is minimal valley fill along the main stem of the Mountain House creek, and the channels that bound the hillslopes are incising into bedrock.

Over 500 shallow landslides occurred during winter storms in 2017 and 90 in 2019 within the 10 km<sup>2</sup> area around our study site (Nelson et al., 2017; Sanders et al., 2019). Most of the shallow landslides (typically less than 100 m<sup>2</sup> in area) liquefied and spread out across lower slopes with only a fraction of the failed sediment reaching active channels (Nelson et al., 2017). Shallow landslides occurred on relatively planar slopes as well as in well-defined hollows. Some, typically located at channel heads, generated debris flows that traveled down canyons.

### 2.3. Soil Description

Soil properties vary with underlying source lithology (sandstone, shale, and conglomerate). In our study area, shale prevails. On the surveyed hillslopes, the soils are thin (typically less than 20 cm) on south-facing slopes and overlie saprolite. These thin soils have abundant sand and gravel saprolite fragments. Based on preliminary field investigation, north-facing slopes have relatively thick soils (locally greater than 1 m), and are finer textured than the south slopes. Macro-porosity associated with biologic disturbance is common, including a weave of grass roots. On both slopes, soil production appears to occur through animal burrowing and root penetration. Soil transport occurs by biogenic disturbance, shallow landslides, and possibly overland flow in extreme runoff events.

### 2.4. Climate

The local climate is Mediterranean, characterized by hot, dry summers and cool, wet winters. Nearly all of the precipitation (534 mm on average annually) falls as rain between October and April (PRISM data, 1981–2020; PRISM Climate Group, 2020), with high inter-annual variability (coefficient of variation of 0.30 between the 2001 and 2018 water years). The mean annual temperature is 15.8°C (PRISM data, 1981–2010; PRISM Climate Group, 2020). The MODIS-inferred mean annual evapotranspiration determined from the Breathing Earth System Simulator (1 km pixel size) from January 2001 to December 2018 was 332 mm (Ryu et al., 2011).

The site did not experience Pleistocene glaciation, but nearby pollen records from Clear Lake in the northern California Coast Ranges suggest this area was 7°C–8°C cooler and wetter (2 m of additional precipitation) during the Pleistocene (Adam et al., 1981; Adam & West, 1983). Periglacial processes may have therefore played a role in hillslope transport processes and soil production.

### 2.5. Vegetation

Vegetation at the site is strongly organized by landscape position including aspect. A ground cover of herbaceous European annuals that senesce in the summer is found across the site, with abundant whitestem filaree (*Erodium moschatum*), California poppy (*Eschscholzia californica*), Fiddleneck (*Amsinckia*), Slender wild oat (*Avena barbata*), Italian thistle (*Carduus pycnocephalus*), milk thistle (*Silybum marianum*), and yellow star thistle (*Centaurea solstitialis*).

Winter deciduous Blue oak (*Quercus douglasii*) savanna-woodland occurs almost exclusively on the north-facing slopes or on primarily east-facing slopes that have a slight northward aspect. Manzanita (*Arctostaphylos*) and toyon (*Heteromeles arbutifolia*) are the only other common woody vegetation in the lower portion study area of the Mountain House watershed, where they are found in association with Blue oak. Prior to European contact, perennial bunchgrasses were likely widespread (Bartolome et al., 1986; Burcham, 1970). Historical air photos obtained from the Santa Barbara Maps and Imagery Library indicate that the present day distribution of Blue oaks was similar in 1937.

## 3. Methods

### 3.1. Approach

We investigate weathering patterns across three unit-hillslopes, one of which is nearly double the ridge-valley spacing of the other two. Westward-draining channels form a boundary condition for the individual hillslope units. We selected a 55-m relief hillslope that defines the divide between the MH7 (catchment

area = 5.2 hectares; Figure 1c) and MH8 drainage (5.9 hectares), and two hillslope units defining the northern (28-m relief) and southern (25-m relief) drainage divide of MH3 (catchment area = 1.8 hectares; Figure 1d). Boreholes were drilled on ridges, slopes, and channels of each hillslope unit to investigate how bedrock weathering varies from ridge to channel.

### 3.2. Topographic Analysis

We based topographic analyses on a LiDAR bare earth digital elevation model (DEM) collected in 2017 with a 0.25 m horizontal resolution and 63 pts/m<sup>2</sup> point density (Dietrich, 2019). To calculate slope (Figure S1), we first performed a bilinear resample of the DEM to 1.0 m horizontal resolution and then calculated slope via the Zevenbergen and Thorne algorithm in QGIS. To calculate curvature, we first performed a bilinear resample on the original DEM to 2 m horizontal resolution, then calculated general curvature via a nine parameter, second order polynomial (the Zevenbergen and Thorne algorithm), then multiplied the output raster by -1. We then smoothed the curvature map twice with a Gaussian filter in circular search mode, with a radius of 3 m and 2 standard deviations, all in QGIS.

To compute summary statistics for multiple catchments as a function of hillslope aspect, we manually drew polygons on the north- and south-facing side slopes adjacent to ridges with boreholes. We include only the planar area of the hillslopes to exclude sandstone outcrops along ridges and channels. We also exclude the artificially steepened slopes along roads in the MH6 and MH7 catchments. We drew these polygon boundaries by visually investigating slope and curvature maps and identifying where the topography transitions from convex to planar (at ridges) and planar to concave (near channels).

To create the map of upslope contributing drainage area (also in Figure S1), we created a smoothed DEM by performing a bilinear resample on the original DEM to 0.5 m horizontal resolution in QGIS, then applying a 2-D median filter over a 10 × 10 m neighborhood with Matlab (R2020a). We then used Matlab to implement the D8 (or steepest descent) algorithm (O'Callaghan & Mark, 1984) to compute the contributing area for each DEM grid cell. After computing hillslope summary statistics, we applied the same 10 m median filter to smooth the slope and aspect maps shown in Figure S1.

### 3.3. Cosmogenic Nuclide-Inferred Catchment-Averaged Bedrock Lowering Rates

We estimated catchment-averaged erosion rates of bedrock by measuring the concentration of <sup>10</sup>Be and <sup>26</sup>Al in quartz in sediments from four basins (from 4 to 137 hectares) within 2 km of the study area (Table S1, Figure S2). The four selected catchments are dominantly soil-mantled, within the Great Valley Sequence, and share similar topographic and vegetative characteristics to our study catchments.

Quartz separation, and chemical and target preparation for three of these samples were performed using standard techniques at the Space Sciences Laboratory (Kohl & Nishiizumi, 1992); one sample, from the MH6 subcatchment, was fully processed at the Prime Lab (Purdue University). The <sup>10</sup>Be and <sup>26</sup>Al measurements for all samples were also performed at the Prime Lab.

We estimated catchment average bedrock lowering rates from the measurements of <sup>10</sup>Be and <sup>26</sup>Al using the CRONUS-Earth online calculators (Balco et al., 2008). In our calculations, we used catchment average elevations that were estimated using the LiDAR DEM and neglected topographic shielding (DiBiase, 2018). We used bedrock bulk densities of 2.65 g cm<sup>-3</sup> and a nuclide-dependent scaling framework (Lifton et al., 2014). Because the catchments are underlain by alternating sandstone and siltstone, there may be spatial variability in quartz content. However, we do not have the data to quantify this variation and expect that the average proportion of siltstone to sandstone remains approximately constant at the catchment scale. We were able to estimate the potential impact of chemical erosion on our estimated bedrock lowering rates via Zr concentrations of recovered samples (Riebe & Granger, 2013; see below). Because Zr enrichment from bedrock to saprolite and soil is small (typically <10%), we do not correct our bedrock lowering rates for this effect.

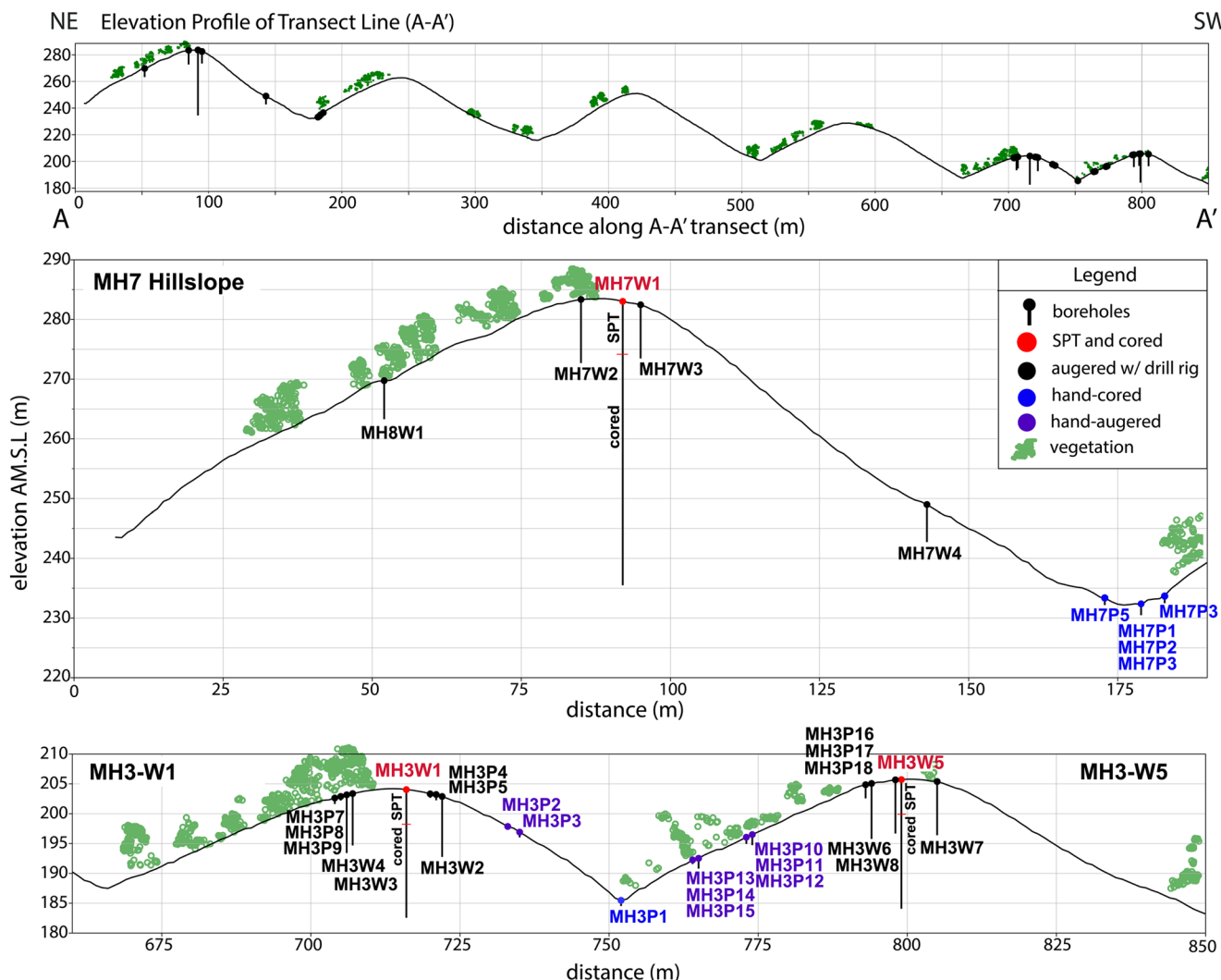


**Figure 2.** Elevation profile of straight-line cross-section A-A' shown in Figure 1b. Vegetation and surface topography are derived from LiDAR. Boreholes are to scale and their color denotes the primary drilling method (see Table S2 for borehole drilling and completion information). Note that these straight-line cross sections differ from the steepest descent cross sections shown in Figure 8.

### 3.4. Drilling

A summary of the borehole drilling methods, including drill type and completion, is illustrated in Figure 2 and available in Table S2. For the three boreholes that penetrate the entire hillslope relief on the ridges, namely MH7-W1, MH3-W1, and MH3-W5, we drilled holes using a combination of standard penetration test (SPT), augering, and, once borehole collapse was no longer a risk, coring. SPT was used to gauge the in-situ strength of the weathered bedrock. The test uses a hollow stem auger that resembles a thick-walled sample tube, with an outside diameter of 50.8 mm, an inside diameter of 35 mm, and a length of approximately 650 mm. This sample tube is driven into the ground at the bottom of a borehole by blows from a slide hammer with a mass of 63.5 kg, falling a distance of 760 mm. As the sample tube is driven into the ground, the number of blows per depth penetrated is recorded.

Shallow boreholes were augered near the deep ridgeline boreholes with a track-mounted auger to an average depth of 9 m (the same rig used for the upper portion of the deep ridgeline boreholes; Table S2). Figure S3 presents a schematic of drilling completion for deep and shallow boreholes drilled on ridgelines. Two additional boreholes were augered on the slopes of MH7 (north-facing: MH8-W1 and south-facing: MH7-W4) to an average depth of six meter. Piezometers located mid-slope and in channels were drilled to an average

depth of one meter using either a human- or gasoline-powered handheld auger (on the hillslopes) or a gasoline-powered handheld core drill (in the channels). During drilling, we documented the relative speed and ease of drilling, core recovery, and the character and color of material retrieved. Discrete fractures and veins were mapped from cores, with the exception of horizontal and jagged fractures that were most likely drilling artifacts.

### 3.5. Downhole Methods

We used an optical borehole imaging (OBI) televiewer to generate a vertically continuous, oriented, 360° image of the borehole wall in the three cored boreholes on the ridgetops (MH3-W1, MH3-W5, and MH7-W1). The OBI is manufactured by Mount Sopris Instruments (model QL40-OBI-2G), and has a vertical and azimuthal resolution of 0.5 and 0.33 mm, respectively. The imagery was limited to the deeper portion of the wells, as the upper 6–9 m were immediately cased to prevent cave-in. Casing extended to the transition in drilling styles from SPT to coring, which also coincided with a reduction in borehole diameter (see Figure S2). We calculated the yellow coloration of each pixel on the borehole imagery as a function of depth following Holbrook et al. (2019) using the formula  $\text{yellow} = (\text{red} + \text{green})/2 - \text{blue}$ . We then averaged across all pixels in horizontal rows to calculate yellowness as a function of depth. The OBI data were used to calculate strike and dip of bedding planes and visible fractures following Serra (1989). The strike was corrected for magnetic declination.

Neutron probe counts (counts per 16 s) were measured in 0.3 m intervals within the unsaturated zone across two surveys in the boreholes (model: CPN 503DR Hydroprobe) bracketing the dry season. Measured changes in neutron probe counts accurately reflect successive temporal changes in volumetric water content (Long & French, 1967) above the water table and therefore provide information about water dynamics in the vadose zone. We deployed pressure transducers to record water level dynamics at 15 min intervals from November 2018 to the present in MH3W1, MH3W5, and MH7W (deep ridgeline boreholes), and from April 2019 to the present in MH3W2, MH3W3, MH3W4, MH3W6, MH3W7, and MH3W8 (augered, medium-depth upper hillslope boreholes). These transducers are offline, internal-battery powered pressure transducers (Solinst Levelogger) that are corrected for atmospheric pressure fluctuations. The accuracy of the Solinst transducers is within 5 mm.

### 3.6. Laboratory Characterization Analyses

Samples from discrete depths were quantitatively analyzed for porosity, color, and chemical composition (~8 g each). 110 samples for geochemical analyses were sent to Bureau Veritas, Inc. (Canada). Samples were first dried and sieved to an 80-mesh for disaggregated samples and a 200-mesh for pulverized core samples. Samples were then heated to measure Loss On Ignition (LOI), and further analyzed via lithium-borate fusion inductively coupled plasma emission spectroscopy (instrument model: Spectro Ciros/Arcos) to obtain total element concentrations. A sub-sample was analyzed for carbon and sulfur concentrations using a LECO CS230. Concentrations of 24 parameters were reported, including major oxides, minor elements, organic and total carbon, and sulfur.

To measure the porosity of matrix chips, we used a helium pycnometer (Micromeritics AccuPyc II 340 Gas Pycnometer) and an envelope density analyzer (Micromeritics GeoPyc 1360 Envelope Density Analyzer) to obtain skeletal and envelope volume, respectively. The skeletal volume includes the solid mineral volume and enclosed or “blind” pores but excludes the interconnected pore spaces within and between mineral grains. In contrast, the envelope volume includes the solid mineral as well as all the pore spaces (both closed and interconnected) within mineral grains, but not the space between mineral grains (or, in this case, rock chips). The skeletal density should always be larger than the envelope density. The Accupyc Gas Pycnometer uses a helium gas displacement method to measure skeletal volume accurately. Helium molecules rapidly fill pores as small as one angstrom in diameter (Micromeritics, 2019a). The GeoPyc Envelope Density Analyzer uses a quasi-fluid with a high degree of flowability that does not wet the sample or fill its pores to measure the envelope volume of the sample (Micromeritics, 2019b). We calculated absolute and bulk density from these measured volumes and the measured sample weights. Porosity values for 195 rock chips were calculated by differentiating absolute density from bulk density. Repeat measurements of a single sample

have a standard deviation of 1.1% while repeat measurements of distinct rock chips from the same depth have a standard deviation of 1.5%.

When weathered, the recovered material that arrived at the surface was commonly a mixture of competent chips of rock and fine-grained material. We analyzed the competent chips of rock for matrix porosity. When competent bedrock core was recovered, we broke off smaller pieces for the matrix porosity analyses. Thus, porosity measurements made on these matrix chips excludes the porosity associated with the fractures or any fine-grained weathering products that occupy fractures. The porosity measurement is only representative of the matrix material that remains intact during weathering.

To quantify color variations with depth, digital photographs of 193 samples at different depths and locations were collected under standardized lighting conditions. The background was filtered out and an average RGB value for each sample was calculated using ImageJ (1.52q).

## 4. Results

### 4.1. Topography, Soil Thickness, and Erosion Rate

On average, north-facing portions of the landscape are less steep (mean hillslope gradient of  $31.2 \pm 5.2^\circ$  standard deviation) than south-facing planar portions of the landscape ( $34.7 \pm 5.2\%$ ). Typical hilltop curvature values along the ridges where the boreholes are located are between  $-0.1$  and  $-0.05 \text{ m/m}^2$  (Figure S1). Similar to hillslope gradient, an aspect-related difference in soil thickness is also present: north-facing slopes tend to have significantly thicker soils (commonly  $>1 \text{ m}$  vertical thickness) whereas soils on south-facing slopes are much thinner ( $0.2\text{--}0.4 \text{ m}$  vertical thickness).

The cosmogenic-nuclide inferred erosion rates are  $72\text{--}131 \text{ m Myr}^{-1}$  close to the study area (Table S1). The ratios of  $^{26}\text{Al}$  and  $^{10}\text{Be}$  concentration ratios in all three catchments close to the study area are consistent with steady-state erosion.

### 4.2. Drilling Observations

At each of the three ridgetops, a single borehole penetrated to a depth corresponding to the entire hillslope relief. Figure 2 shows the location of all 35 boreholes drilled across our three study hillslopes and Table S2 documents the depths, and drilling and completion details.

#### 4.2.1. Bedding and Fracture Characterization

The strike and dip of bedding observed in the borehole imagery (Figures S4b and S4c) are  $330 \pm 7^\circ$  and  $52 \pm 3^\circ$ , generally consistent with measurements in local bedrock exposures and the geologic map (Rich, 1971) of the study site (dips of  $54^\circ$  and  $55^\circ$  and strikes that were also oriented closer to north, of  $351^\circ$  and  $340^\circ$ ). The optical imagery did not reveal a significant difference in bedding orientation between boreholes (Figures S4b and S4c). Each borehole intersects a unique sequence of beds, with the exception of likely overlap in the lower eight meters of MH3-W5 and upper eight meters of MH3-W1 as determined by the projection of the strike of each borehole to surface topography shown as lines in Figure S4.

Borehole imagery reveals repeated layers of varying thicknesses of shale and sandstone beds (OBI in Figure 3). Most of the transitions between beds tend to be abrupt and occur within several centimeters, with  $\sim 10$  transitions per vertical meter between sandstone and shale, corresponding to an overall average bed thicknesses of about 10 cm. There is significantly more shale than sandstone, particularly at MH3-W5 and the lowest 20 m of MH7-W1.

For the three ridgeline boreholes, Figure 3 shows vertical profiles of color (RGB), blow counts (SPT), OBI-determined yellowness and fracture traces, and the unwrapped OBI image. We describe how these data are used to identify four layers: mobile soil, pervasively fractured bedrock, discretely fractured bedrock, and rarely fractured bedrock (example photos shown in inset of Figure 3).

The interface between the soil layer and pervasively fractured bedrock is visible in roadcuts and soil pits (see, e.g., Figure S5). Soils are physically disturbed, disaggregated, and mobile, while the underlying pervasively fractured bedrock retains its relic structure (e.g., bedding, Figure 3, inset photo). The transition

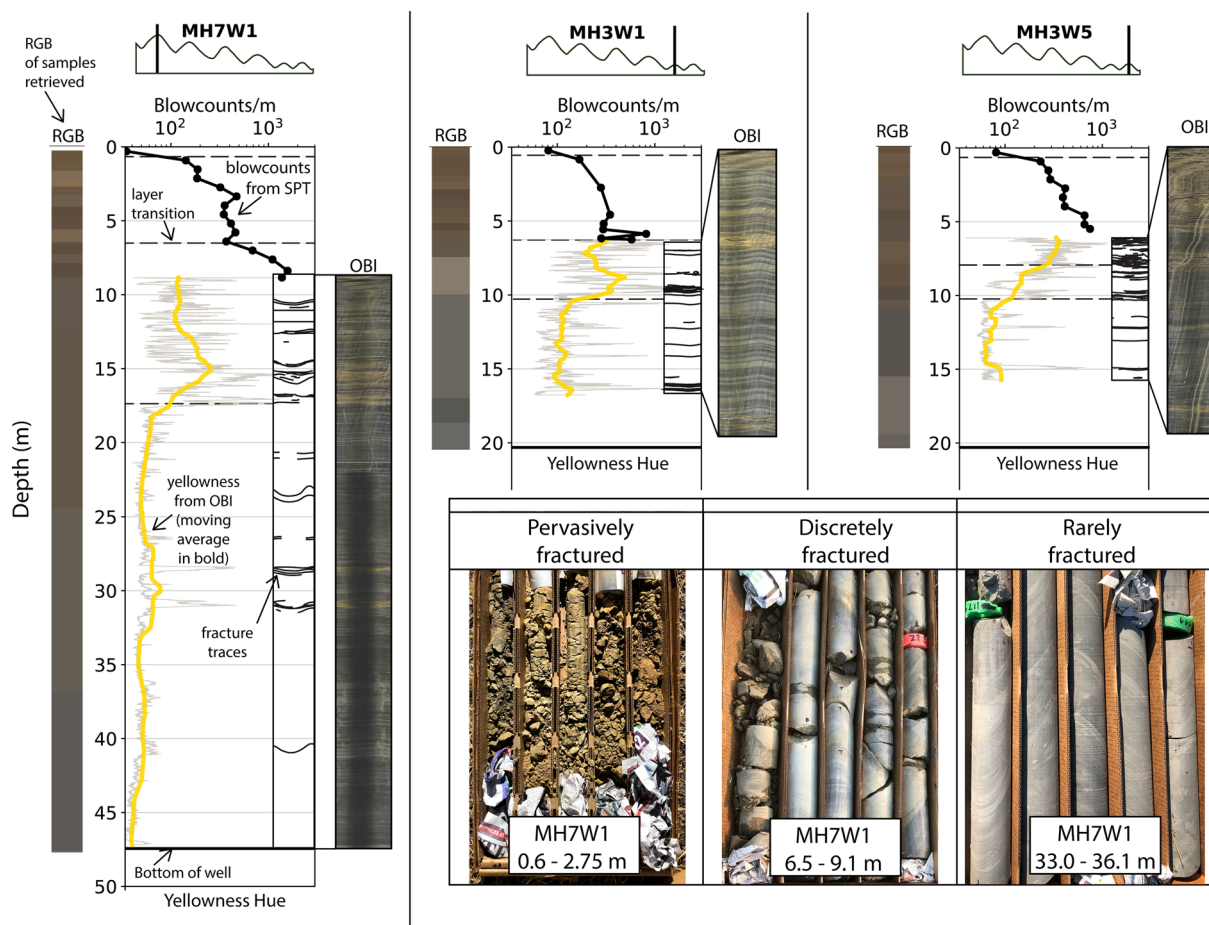


**Figure 3.** Fracture and color characterization of three ridgeline boreholes. Vertical profiles, from left to right, are shown for the color (RGB) of samples retrieved, blow counts, yellow hue from optical borehole images, fracture traces and the unwrapped view of optical borehole imagery (OBI) logs. Yellow hue is shown as a gray line overlaid by a moving average in yellow. Blow count data are limited to depths above coring, and fracture trace and yellow hue data are limited to depths where OBI data were collected. Example photos of pervasively fractured bedrock, discretely fractured bedrock, and rarely fractured bedrock are shown in the bottom right inset.

between soil and the pervasively fractured layer is equivalent to the soil-saprolite boundary. We do not attempt to define a base of saprolite, but it lies somewhere within the pervasively fractured layer. This soil to pervasively fractured bedrock transition is located at <0.25 m for MH7-W1, and at 0.45 m for both MH3-W1 and MH3-W5. An abrupt increase in blow counts occurs at the base of the mobile soil layer (Figure 3). The pervasively fractured bedrock is mechanically weak, as evidenced by the ease of penetration (see blow counts in Figure 3). Samples recovered via augering and SPT at these depths are discolored and iron stained (Figure 3, inset photo). Blow counts generally increase with depth throughout this zone. Fracture density observed in recovered samples is greater than 50 fractures per meter.

The discretely fractured bedrock layer is characterized by discrete fractures or fracture zones separated by relatively intact bedrock that shows minimal signs of oxidation (Figures 3 and 4). Fracture density is approximately three fractures per meter (Figure 3) and material recovered from fractures or fracture zones can be fine-grained and highly weathered. The yellowness calculated from OBI imagery captures the weathering and iron staining observed in core samples. This allows us to use yellowness as a proxy for weathering in Figure 3.

The transition from pervasively to discretely fractured bedrock was marked by changes in mechanical strength. At MH7-W1, the transition occurred at a relatively abrupt increase in blow counts at 6.5 m. At MH3-W1, the transition was marked by an abrupt decrease in the rate of augering (by gas powered track-mounted drill rig), which necessitated a change in drilling method to coring. In MH3-W5, the

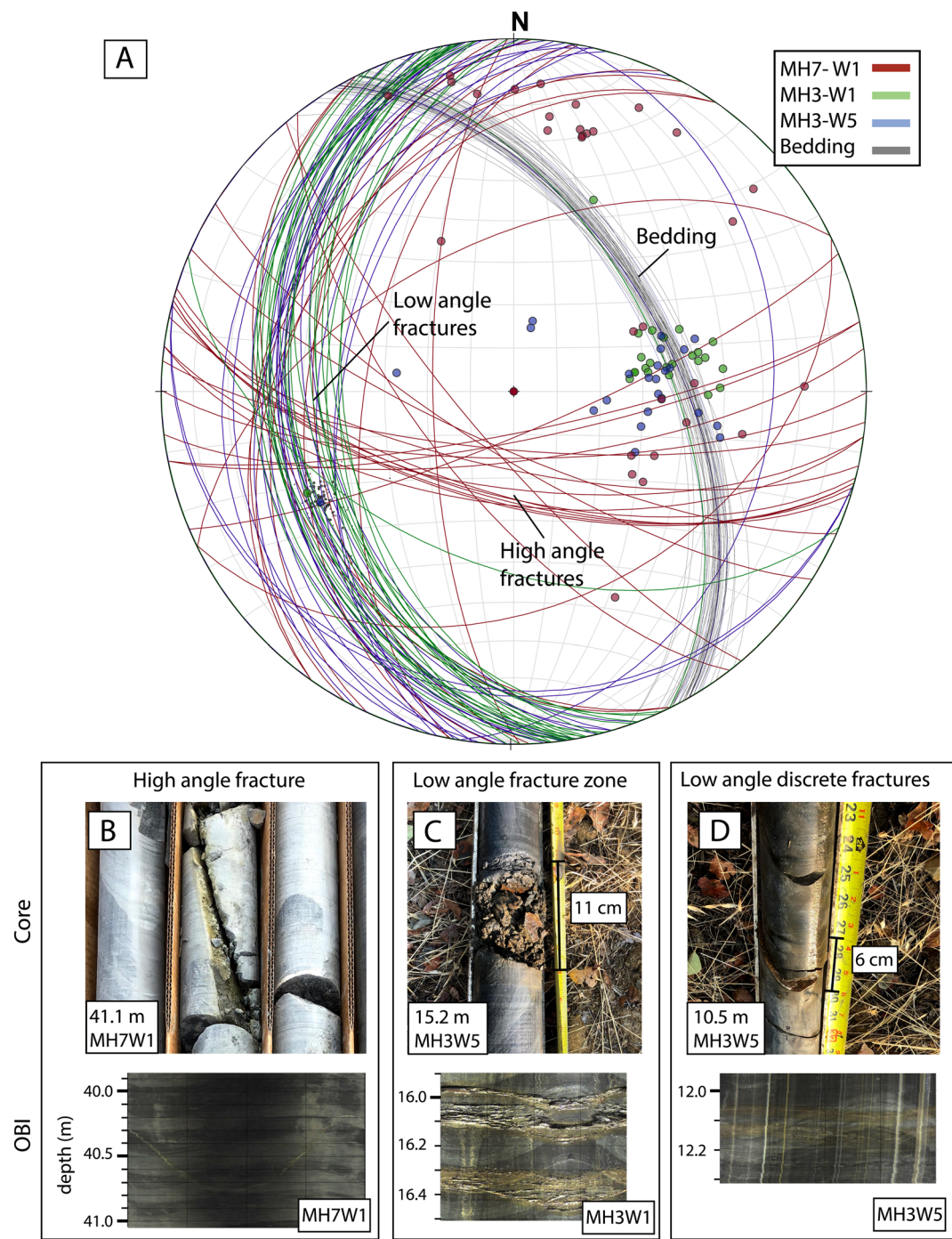


**Figure 4.** (a) Stereonet of fractures (colored by borehole) and bedding planes (gray) identified in OBI logs (lower hemisphere projection). Expression of different fracture types in core and OBI are shown in (b–d), where two dominant fracture orientations are identified: high angle fractures and low angle fractures. Unwrapped OBI images show dipping, alternating sandy and fine-grained units intersected by fractures that cut across bedding.

transition occurred at 7.5 m depth, shortly after the transition to coring, and was marked by an abrupt decrease in fracture density.

The transition from discretely fractured to rarely fractured bedrock is associated with a decrease in both fracture density and yellowness. In the rarely fractured zone, fractures are discrete and often cemented.

Individual fractures are separated by continuous, meters-long sections of dark-hued, unoxidized bedrock that lack evidence of weathering.

Fractures and fracture zones throughout the profile do not appear to be associated with any particular stratigraphic unit or confined to individual beds. Instead, fractures and fracture zones crosscut bedding planes, and fracture zones can include both shale and sandstone beds (Figures 4b–4d). In the OBI, sandstone beds stand out as being iron stained or discolored more so than shale beds (Figure 3). However, core samples reveal that, within fracture zones, both shale and sandstone are weathered and there does not appear to be a dominant bedrock type within which weathering is concentrated.

Two dominant types of fractures are present: high angle ( $60\text{--}80^\circ$  dip) fractures oriented at a strike of  $\sim 97^\circ$  and low angle ( $30\text{--}40^\circ$  dip) fractures oriented at a strike of  $\sim 172^\circ$  (right-hand rule convention; Figure 4). Low angle fractures appear as both discrete fractures and fracture zones, whereas high angle fractures tend to be primarily discrete (Figures 4b–4d). High angle fractures are present in the core recovered from all three ridgeline boreholes and they are distributed relatively evenly throughout the depths cored. In contrast, low angle fractures generally increase in abundance toward the surface. Fractures become more abundant and more open toward the surface, while fractures at depth are closed and often stained. The fractures identified in the OBI and core are consistent with the joint set measurements in the shale unit along the Freshwater Creek beds (Figure 1b).

The color of recovered material for augered hillslope boreholes and channel piezometers is summarized in Figure 5. Drilling of augered hillslope boreholes ceased when it was qualitatively determined that the speed of drilling had slowed down significantly and the character of the material recovered was consistently gray in color, lacking signs of oxidation. Throughout each profile, distinct, progressive changes in color and texture occur. A gradual darkening in brown is observed in deeper samples, transitioning to a very dark brown, and in most wells, transitioning to a dark gray at the base. In channel piezometers, which were cored, dark-colored, competent bedrock was encountered within the first 0.5 meter. The cores from the channels were similar in composition and extent of weathering as cores characteristic of discretely fractured or rarely fractured bedrock (Figures 3 and 5, inset photos).

#### 4.3. Porosity, Sulfur, and Carbon in the Bedrock Matrix

Depth profiles of matrix porosity, sulfur concentration, organic and inorganic carbon concentration, and seasonal rock moisture for the boreholes drilled on the ridgelines, channels and side-slopes are shown in Figure 6. Matrix porosity refers to the porosity of matrix chips in the fractured and weathered bedrock and therefore does not include porosity associated with the fractures that bound the bedrock matrix. An average of matrix porosity of samples from the same depth is shown in Figure 6, with the exception of one data point with a standard deviation  $>5\%$ .

The matrix porosity of samples from the rarely fractured bedrock layer, which is chosen to represent unweathered parent material, ranges from 5.0% to 7.4%. The matrix porosity of samples at shallow depths ( $<2$  m) below the channels and at depths ( $>15$  m) at the ridgelines is comparable to the matrix porosity of parent material. Above 10 m depth at the ridgelines, matrix porosity typically exceeds 10%, and can exceed 20% in some places. Matrix porosity of the MH7 ridge samples is generally greater than in the MH3 ridgelines at equivalent absolute depths. Matrix porosity on the south-facing hillslope (MH7W4, which is at a lower relative elevation and closer to the channel), is consistently lower than the north-facing hillslope (MH8W1, which is at a higher relative elevation and closer to the ridge).

We use sulfur concentrations to represent the presence of pyrite to identify a pyrite weathering front. The trend of sulfur with depth at the ridges tends to be binary: sulfur is not detectable above a particular depth and tends to have a variable but detectable concentration below, typically around 0.3%, with maximum observed concentrations of 2.0%. The method detection limit for sulfur is 0.02%. Sulfur is not detected above 5.7 m depth at the MH7-W1 ridge, 7.1 m depth at the MH3-W1 ridge, and 9.1 m depth at the MH3-W5 ridge; the first incidence of sulfur is denoted by a horizontal dashed black line in Figure 6. In contrast, detectable sulfur concentrations are found at significantly shallower depths in the channel samples (at 1.9 and 1.0 m depth in the MH7 and MH3 channels, respectively). The pyrite dissolution fronts in mid-slope boreholes are comparable to those of the ridgeline boreholes, at  $\sim 5$  and 7 m depth for MH7-W4 and MH8-W1, respectively.

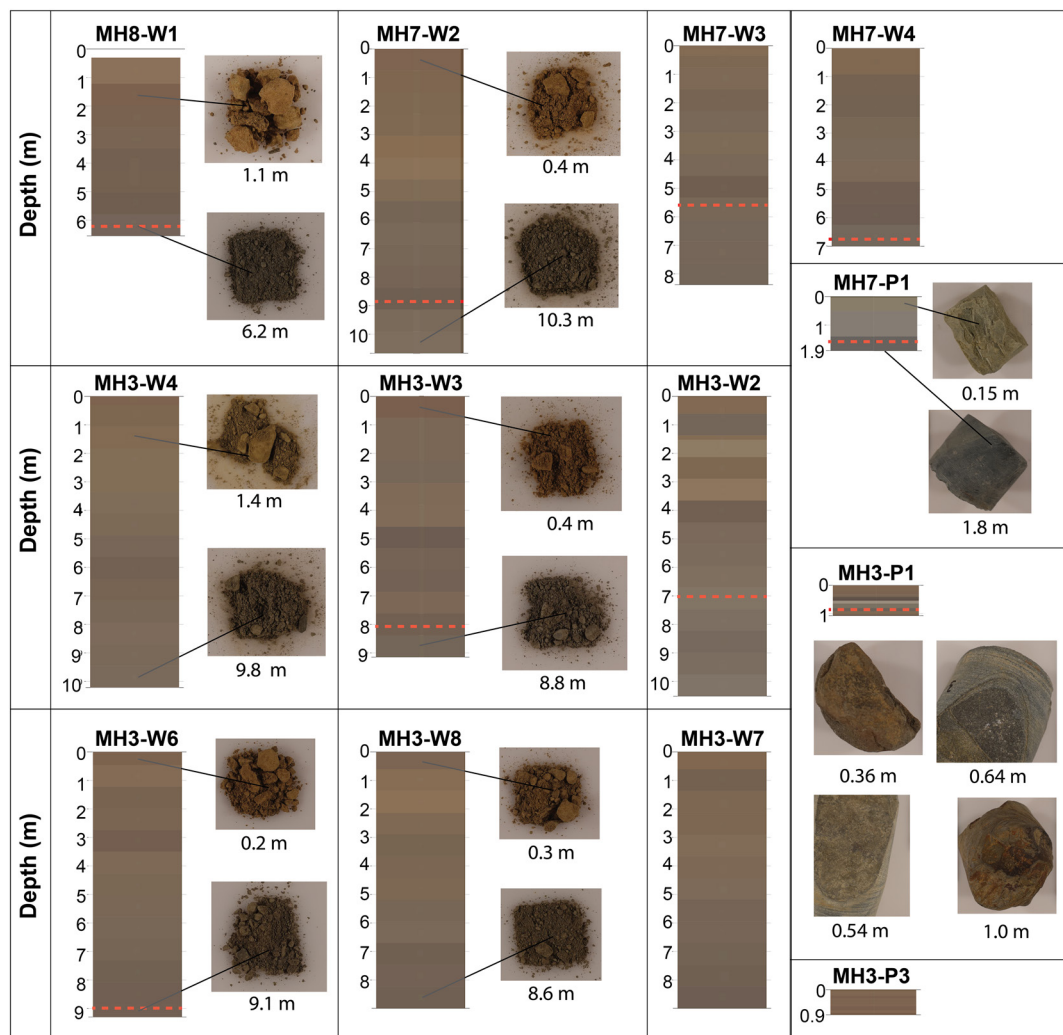


**Figure 5.** Depth profiles of color (RGB from digital photographs). Example photographs of material are shown. The red dashed lines, where present, mark where the pyrite oxidation front is located in each borehole (see Figure 6).

Vertical profiles of inorganic carbon (Figure 6), and calcium concentrations (Figure 7) of matrix chips do not provide strong evidence for the presence of a carbonate dissolution front. There are low concentrations of calcium and inorganic carbon, and thus little carbonate mineral, in the parent material. Inorganic carbon (Figure 6) and calcium (Figure 7), which scale with one another, are highly variable throughout the profile and do not show a systematic pattern with depth. By applying hydrochloric acid to the core during drilling, several discrete veins and calcite rich beds were identified, but the core was not systematically mapped for carbonates. While inorganic carbon and calcium concentrations in the matrix chips analyzed range from 0% to 1.0% and 1.0% to 4.9%, respectively, three of the samples analyzed for bulk chemistry showed distinctly high inorganic carbon (1.6%–4.4%), high calcium (8.0%–17.3%) and low silica (14.9%–20.1%). These samples (from MH3-W1 at 7.5 m, MH3-P1 at 0.59 m, and MH7-W1 at 24.4 m) are likely associated with discrete carbonate-rich beds or veins and are excluded from Figures 6 and 7.

In the ridgeline and hillslope boreholes, organic carbon first decreases with depth within the upper four meters and then increases with depth. The higher organic carbon concentrations in the very shallow near surface are likely related to modern organic carbon associated with the soil and rhizosphere. At great depth, the organic carbon concentration of the parent material is ~1.0%–2.0%, and decreases toward the surface, dropping from maximum concentrations of about 2.0% to about 0.5%, likely reflecting loss through oxidation. Organic carbon concentrations in the MH7 and MH3 channels are high (0.75%–1.0%) relative to the

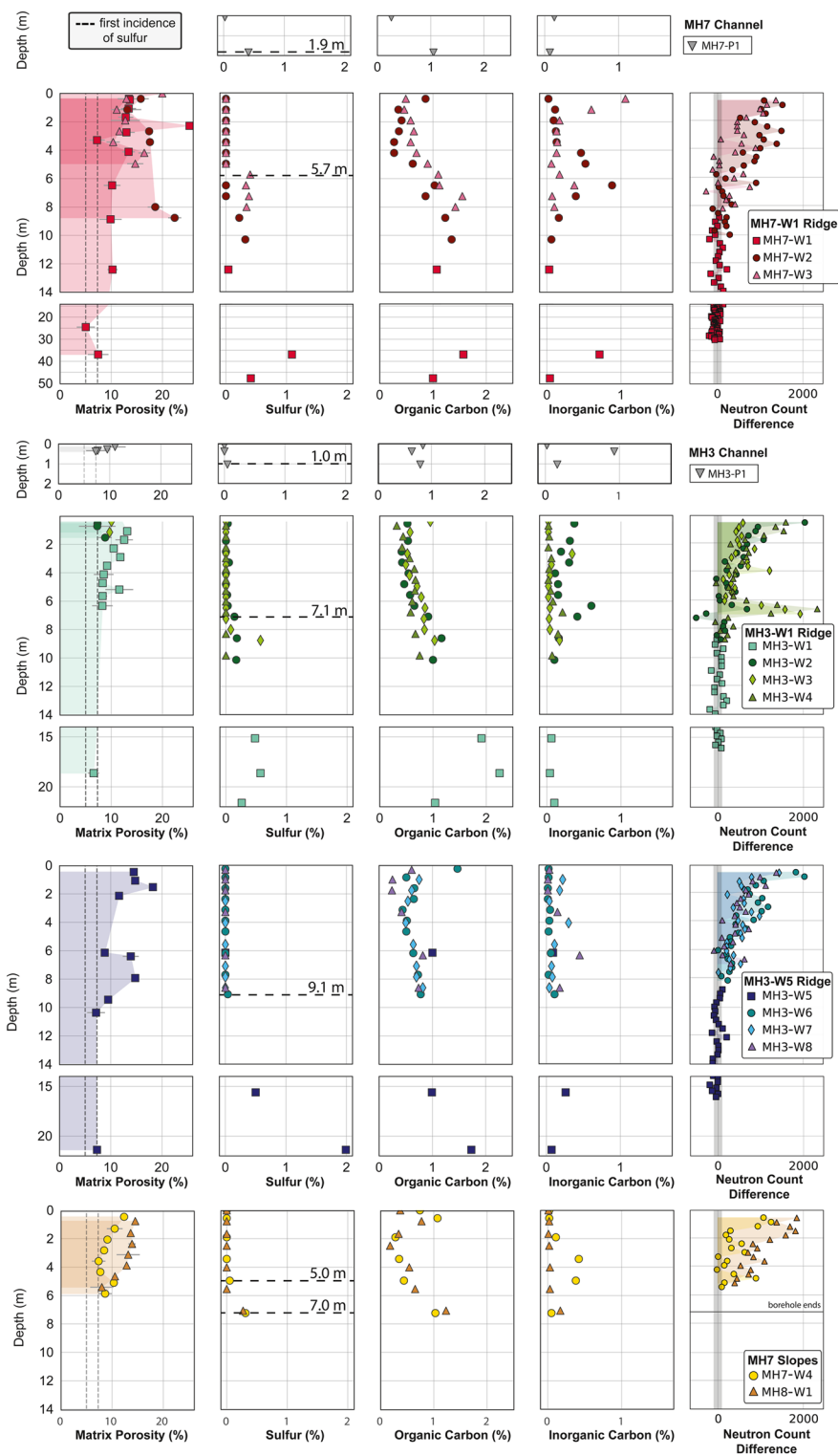


**Figure 6.** Characterization of porosity, oxidation fronts and rock moisture. Depth profiles (from left to right) illustrate: matrix porosity of recovered chips (left-most column), sulfur concentration (center-left column), organic carbon concentration (center column), inorganic carbon concentration (center-right column), and neutron count difference (right-most column). Each row is a group of samples collected from boreholes in a particular location (ridgetop, side-slope or channel). Note break in vertical scale below 14 m for ridgetop samples. Vertical lines in matrix porosity plots show range of porosities in unweathered bedrock. Horizontal dashed lines in sulfur plots show depth to first significant appearance of sulfur. Neutron count difference points show seasonal change (from wettest to driest state) in neutron counts, a proxy for unsaturated zone volumetric water content. Vertical shaded band shows typical range of measurement uncertainty of the neutron moisture gauge.

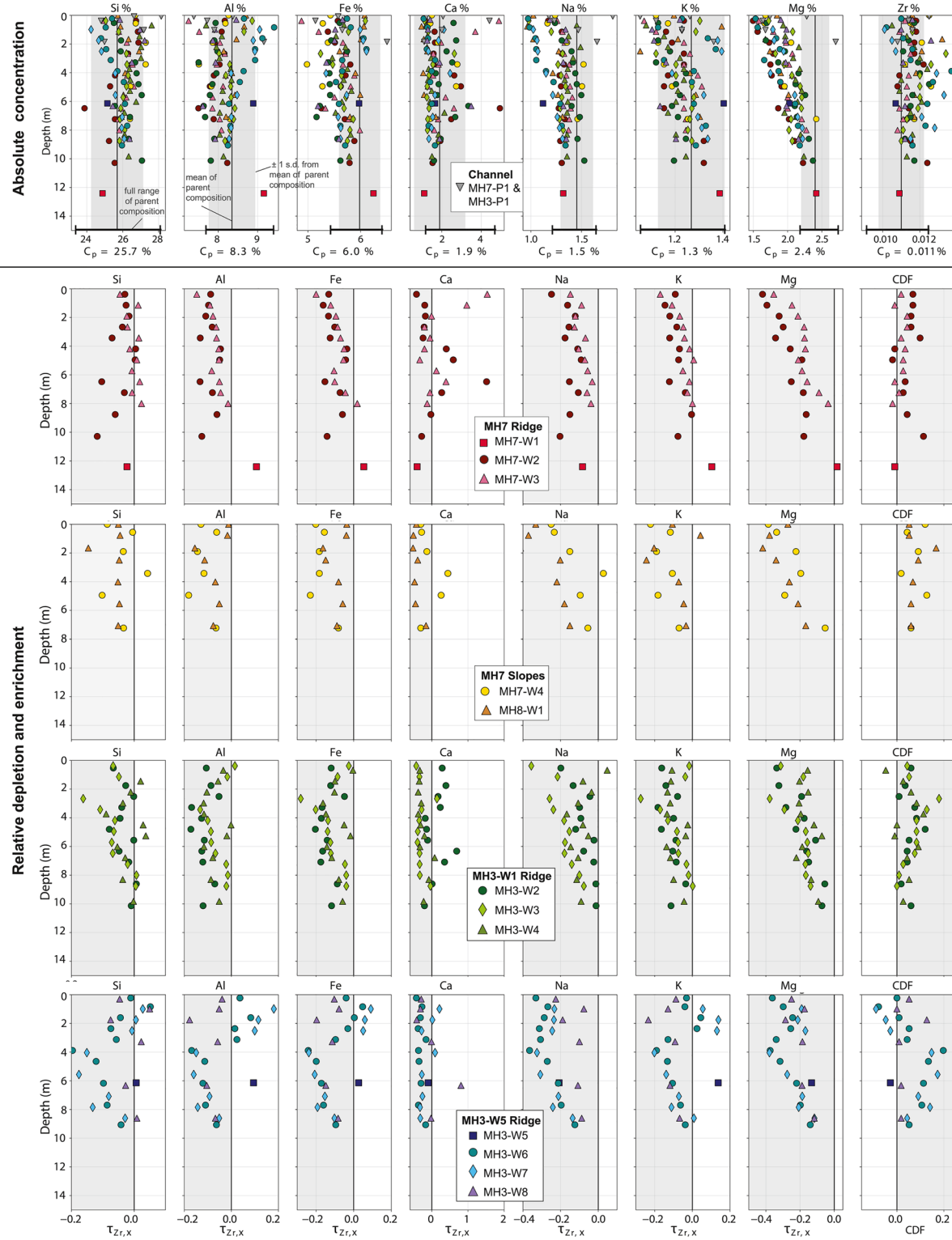


**Figure 7.** Top row: Absolute geochemical composition of samples from the upper 15 m (points). Typical parent material compositions ( $C_p$ ) of samples  $>15$  m are noted in each subplot title (mean) and shown via vertical black line and light gray bands (mean  $\pm 1$  s.d.); bar at bottom shows minimum-maximum range of parent material. Lower rows: chemical depletion/enrichment plots of individual elements, expressed as  $\tau$  (tau), and overall samples, expressed as the chemical depletion fraction (CDF), grouped by geographic area and landscape position (individual rows). Note distinct abscissa axis scales between elements for the  $\tau$  plots. Shaded regions in tau profiles and CDF indicate depletion.

concentrations measured at similar depths in the ridgeline boreholes, and are most similar to rarely fractured (parent) samples in the ridgeline boreholes. The depth profile of organic carbon is relatively consistent across the MH7 hillslope.

#### 4.4. Chemical Weathering Patterns of Major Rock-Forming Elements

The top panel of Figure 7 illustrates depth profiles of the absolute concentration of the major rock-forming elements as well as Zr. Individual points are colored by their borehole. The vertical gray bands indicate the mean  $\pm 1$  standard deviation of unweathered parent material composition and the horizontal line along the x-axis marks the total range of parent composition. The parent material is defined by seven bedrock samples taken from the rarely fractured, deep, cored ridgeline boreholes. All these parent material samples were located deeper than 15 m. In general, the parent material elemental concentration is highly variable (the width of the gray vertical bands is equal to two standard deviations), and is comparable to the variation in elemental composition in the upper 15 m. The individual elemental concentrations tend to have greater variability at surface than at depth (Figure 7). Above the parent material, K, Mg, and, to a lesser extent, Na, generally decline in concentration toward the surface, while Si, Al, Fe, Ca, and Zr do not show a systematic pattern with depth. Concentrations of Si and Zr tend to be higher in the upper 15 m relative to parent material (most points are to the right of the vertical black line), whereas concentrations of Al, Fe, Ca, Na, K, Mg tend to be lower than the parent material.

To track gains and losses of individual elements relative to the parent material, concentrations in the weathered profile are typically compared to chemically less-mobile elements (e.g., Zr, Ti, and Nb), under the assumption of a common starting parent material chemical elemental composition (Brimhall & Dietrich, 1987; Nesbitt, 1979; Riebe et al., 2017). Figure 7 illustrates depth profiles of individual elements' enrichment or depletion using Zr as an immobile reference element, expressed as  $\tau$  (tau) for individual elements. Strain calculations (i.e., Brimhall & Dietrich, 1987) were not performed given that the samples sent for elemental analysis differed to those used for porosity measurements. The modest dissolution losses and porosity change suggest that strain is minor.

Equation 1 expresses the weathering-related mass loss in fractional terms, relative to the amount of the element that was present in the protolith as  $\tau_x$ , the "mass-transfer coefficient" for element X (Anderson, Dietrich, & Brimhall, 2002; Brimhall & Dietrich, 1987). Here,  $I$  is the concentration of an immobile element and the subscripts regolith and protolith in both equations refer to the type of material which element concentrations are measured in, either weathered (regolith) or unweathered (protolith).

$$\tau_x = \frac{X_{\text{regolith}} I_{\text{protolith}}}{X_{\text{protolith}} I_{\text{regolith}}} - 1 \quad (1)$$

The chemical depletion factor (CDF) is reported for each sample as a whole and is expressed in Equation 2 (Riebe et al., 2017).

$$CDF = 1 - \frac{I_{\text{protolith}}}{I_{\text{regolith}}} \quad (2)$$

Under the assumption that Zr is chemically immobile and the parent material compositions are representative, a  $\tau_{Zrx}$  value of  $-0.1$  indicates a 10% decrease of an element relative to its initial abundance in the parent material; a value of  $0.1$  indicates a 10% increase relative to its initial abundance in the parent material. A CDF value of  $0.1$  indicates that 10% of the sample's entire mass has been lost chemically relative to the initial parent material.

Most elemental  $\tau_{Zrx}$  plots show significant scatter without clear patterns in the upper 10 m as a function of depth. However, Mg, K, and Na tend to be more depleted closer to the surface (Figure 7). The majority of samples have negative  $\tau_{Zrx}$  values (plotting in the gray shaded region left of the vertical line), indicative of chemical depletion; this is consistent with the overall CDF values for the samples as a whole, which tend to be variable but positive. Negative  $\tau$  values are observed for both Fe and Al within the weathered bedrock zone, both of which are typically considered to be relatively immobile. Depletion of Ca, a relatively mobile

element, is also observed throughout the weathered profile. Approximately 10% (up to a maximum of 20%) of the original starting mass of samples in the weathered zone has therefore been lost to chemical erosion. These inferred mass losses are consistent with the inferences from the matrix porosity, which are similarly variable but also indicate a 5%–15% gain in porosity from parent material to weathered material.

#### 4.5. Water Storage

Colored points on the right-most column of Figure 6 illustrate the dynamic storage of water in the vadose zone as the difference in neutron counts from the wet season (measurement date March 19, 2019) to the dry season (measurement date February 11, 2019). Moisture is lost and gained seasonally in the locations that experience neutron count change. The largest seasonal dynamic occurs closest to the ground surface and decreases with depth until the observed difference is indistinguishable from the sensitivity of the instrument (denoted with the vertical gray band). The depth of seasonal moisture dynamics is 7–8 m for the MH3 and MH7 ridgetops and 5 m for the boreholes on the slopes of MH7. These measurements followed a significantly wetter-than-average wet season, in drier years, it is possible that the dynamic rock moisture change is neither as deep nor as large. A significant fraction of the deeper vadose zone does not exhibit a measurable change in water content.

Water levels in deep boreholes were observed to depths of 33.9 m at MH7W1, and 19.5 and 20.4 m at MH3W1 and MH3W5 respectively. These boreholes are continuously slotted below depths of 11 m in MH7W1, and 6 m in MH3W1 and MH3W5. Therefore, the water level in the borehole may not reflect the elevation of the water table within the hillslope. Our borehole completion and groundwater monitoring did not allow us to document hydraulic head or hydraulic gradients. Nonetheless, we can conclude that the water table must be deeper than 2.5 m, due to the lack of water in five piezometers spanning mid-slope to ridge top positions in MH3, over the time period spanning the beginning of December 2018 to the end of February 2019, which included a large storm sequence.

#### 4.6. Summary of Weathering Fronts

Taken together, our datasets reveal that below a shallow soil-weathered bedrock boundary (labeled Interface 1 in Figure 8), lie two distinct weathering fronts. Beneath all ridges, the two fronts are separated by several meters, while under the channels, the two fronts coincide. Above the shallower weathering front (“Interface 2”; Figure 8) there is a loss of pyrite, organic carbon, and mechanical strength relative to the underlying bedrock. The bedrock matrix is weathered and shows measurable mass loss and increased porosity (Figure 7). Interface 2 coincides with the transition from pervasive to discrete fracturing (Figure 3). The bedrock between Interface 2 and the deeper weathering front (“Interface 3”; Figure 8) has fewer fractures that are less open. The bedrock matrix between fractures is not as visibly weathered as the bedrock above Interface 2, and borehole imagery reveals a decrease in yellow coloration of the bedrock across Interface 3 (Figure 3), suggesting some chemical alteration of the bedrock matrix between Interfaces 2 and 3. Below Interface 3, the bedrock is rarely fractured and fractures are dominantly closed.

The depth of Interface 2 is similar across all three ridges (6.3–7.5 m, Table 1). The depth of Interface 3 is significantly deeper for MH7-W1 (17.5 m) relative to MH3-W1 and MH3-W5 (11 and 10.5 m, respectively) (Table 1). The relief of each interface (i.e., the difference in elevation between the interface height and the channel bed elevation following the path of steepest descent from the ridge) is reported in Table 1 and compared to the hillslope length and topographic relief in Figure 9. This relief is taken at the ridgeline. Because the calculation of length and relief vary on the north and south side of each ridge, the relief is reported for north and south sides of the hillslope separately in Table 1. Figure 9 illustrates that the relief of the ground surface and the weathering fronts scale approximately linearly with hillslope length.

### 5. Discussion

#### 5.1. Water Storage in Weathered Bedrock

Water storage in the weathered bedrock unsaturated zone (rock moisture) is seasonally dynamic to depths of 5–8 m. This moisture likely serves as an important water source to vegetation during the extended dry

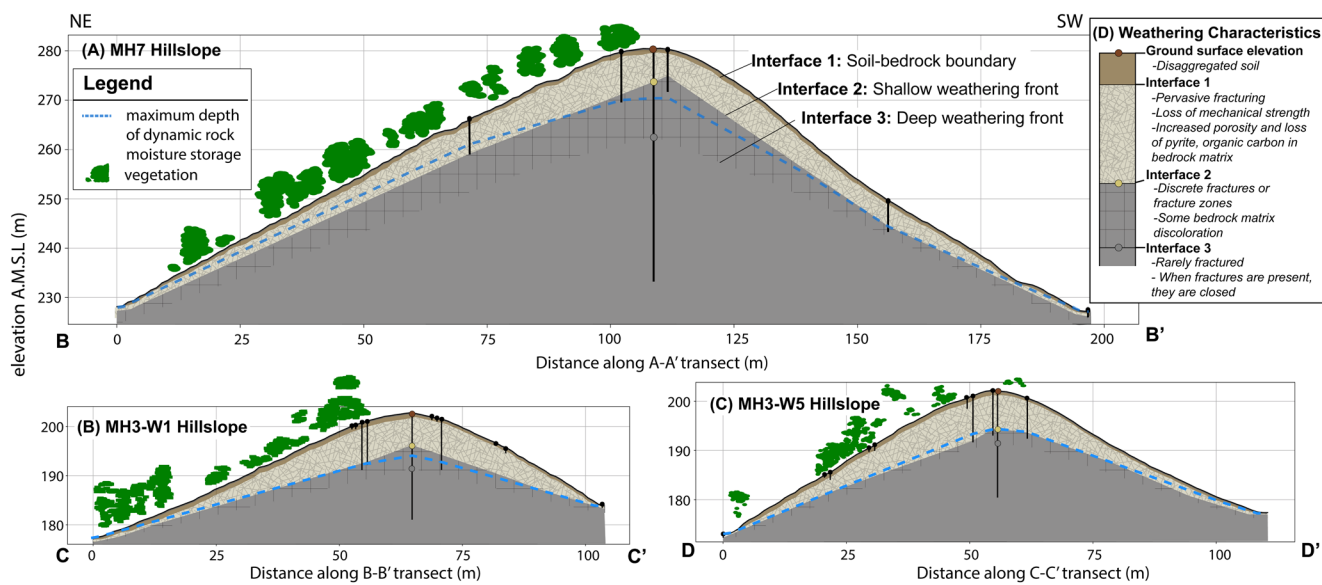


**Figure 8.** The spatial pattern of weathering fronts and moisture storage across three study hillslopes (a–c). Vegetation and surface topography are derived from LiDAR data. Cross-sections locations are shown in Figures 1c and 1d, and are aligned with the steepest descent of topography as opposed to the straight line cross-section used in Figure 2. Borehole locations are shown as vertical black lines and weathering interfaces are linearly interpolated between observations made at boreholes, but could take a number of forms. Interface locations at ridgetop boreholes are shown as colored circles. The maximum depth of dynamic rock moisture storage is shown as a blue dashed line. Inset D illustrates the weathering profile characteristics.

season. It is not evident whether rock moisture is accessed from fractures or bedrock matrix pore domains, but it is likely that the larger pores present in fractures would serve as the dominant water transmission pathways for deep penetration of water into the bedrock vadose zone. We therefore hypothesize that the seasonal dynamics are likely confined to fractures, while the smaller bedrock matrix pores remain at or close to saturation year-round.

The location of water storage dynamics in the hillslope did not appear to be confined to individual beds or a particular lithology across our study hillslopes. Although dynamic rock moisture occurs predominantly above Interface 2, in some instances, Interface 2 extends below the depth of detectable rock moisture dynamics (Figures 6 and 8). This suggests that rooting depth may not correspond with a weathering front depth.

**Table 1**

*Length (L) of Study Hillslopes and the Relief of the Topographic ( $Z_s$ ) and Weathering Surface ( $Z_b$ )*

Hillslope	L (m)	$Z_s$ (m)	$Z_s/L$	Interface 2				Interface 3			
				Depth to $Z_2$ (m)	$Z_2$ (m)	$Z_2/L$	$Z_2/Z_s$	Depth to $Z_3$ (m)	$Z_3$ (m)	$Z_3/L$	$Z_3/Z_s$
MH7 North	111.2	52.4	0.47	$6.5 \pm 0.8$	45.9	0.41	0.88	17.5	34.9	0.31	0.67
MH7 South	85.9	53.1	0.62	$6.5 \pm 0.8$	46.6	0.54	0.88	17.5	35.6	0.41	0.67
MH3-W1 North	64.4	25.3	0.39	$6.3 \pm 0.8$	19	0.3	0.75	11	14.3	0.22	0.57
MH3-W1 South	39.4	18.6	0.47	$6.3 \pm 0.8$	12.3	0.31	0.66	11	7.6	0.19	0.41
MH3-W5 North	54.4	29.2	0.54	$7.5 \pm 1.6$	21.7	0.4	0.74	10.5	18.7	0.34	0.64
MH3-W5 South	56.1	25	0.45	$7.5 \pm 1.6$	17.5	0.31	0.70	10.5	14.5	0.26	0.58

$Z_2$  and  $Z_3$  represent two instances of  $Z_b$  for Interface 2 and 3, respectively. Relief is measured from the adjacent channel at the topographic divide. Given the asymmetry of our study hillslopes, length and relief are reported for both north and south sides of the hillslope. Fractional relief of the hillslope that remains unweathered at the hillslope divide ( $Z_b/Z_s$ ), the mean slope of the surface elevation ( $Z_s/L$ ) and fresh bedrock elevation ( $Z_b/L$ ) is calculated for each hillslope.

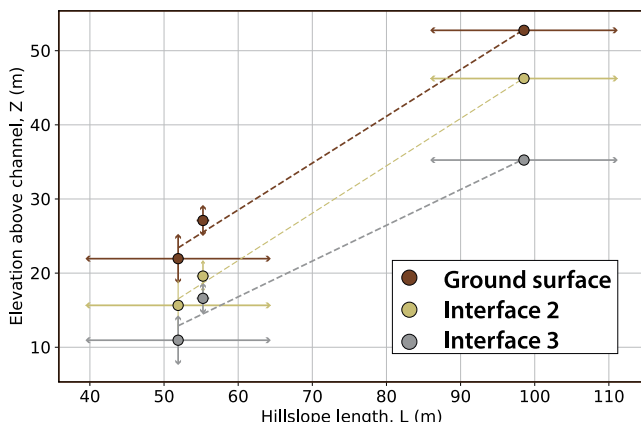


**Figure 9.** Relationship between hillslope length and relief of the ground surface and the two weathering fronts shown in Figure 8. Points represent length or relief averaged across both north and south sides of the hillslope. Error bars represent the full range of relief or length calculated for each side of the hillslope. The dashed lines represent ordinary least squares best fit lines.

Wan et al., 2019; Gu et al., 2020). Pyrite oxidation could be limited within the vadose zone if the bedrock matrix remains saturated or if reactive potential is exhausted at shallow depths within the vadose zone. Diffusive transport of oxygen to the interior of large, poorly fractured matrix blocks could occur slowly enough above the water table to limit oxidation. Fracture spacing in this case would play a role in the pace of oxidation (Reis & Brantley, 2017). Reactive transport modeling results indicate that under sufficiently low infiltration rates the water table can be deeper than the position of oxidative weathering fronts (Lebedeva & Brantley, 2020). Further work at the site is needed to evaluate the relationship between the water table elevation, reactive potential in the vadose zone, and the location of the pyrite oxidation front.

The oxidation of rock-organic carbon is another commonly observed weathering reaction in shale (Wan et al., 2019; Wildman et al., 2004) that, alongside silicate weathering, plays a role in the global carbon cycle (France-Lanord & Derry, 1997). The organic carbon oxidation front has a similar depth penetration but is more gradual than pyrite (Figure 6), with relatively high organic carbon concentrations remaining at locations where pyrite is absent and assumed to be oxidized. This suggests that under the same weathering conditions, pyrite oxidizes faster than rock organic carbon. This finding is consistent with other weathering studies including the New Albany shale in Kentucky (Wildman et al., 2004), the Mancos shale in Colorado (Wan et al., 2019), and the Rose Hill shale in Pennsylvania (Brantley, Holleran, et al., 2013).

Relative to pyrite and organic carbon, we found it difficult to locate a carbonate reaction front (Figure 7). This may be due to cyclic dissolution and re-precipitation of calcite (similar to Wan et al., 2019), the heterogeneous distribution of calcite within different beds, or our low sampling frequency which may have missed isolated carbonate features. Overall chemical losses (see CDF, Figure 7) are observed but are highly variable in the upper 15 m. This variability is likely a product of the relatively large variation in parent-material composition of both the assumed immobile reference element, Zr, and the other individual primary rock-forming elements themselves. The observed geochemical heterogeneity at great depth suggests that the individual interbeds in the weathered bedrock also had heterogeneous parent compositions. Further work is needed to determine how and if variations in grain-size can be used to improve interpretations of chemical depletion profiling in sedimentary systems. Nevertheless, we observed some abrupt and gradual chemical

## 5.2. Controls on the Location of Reaction Fronts and Fractures

The depth and sharpness of individual reaction fronts are widely used to describe weathering patterns (Brantley & Lebedeva, 2011). In shale, both pyrite oxidation and carbonate (e.g., calcite) dissolution are recognized as key diagnostic fronts. Pyrite oxidation results from atmospheric oxygen delivery to bedrock. The pyrite oxidation front (defined here as the transition between undetectable to detectable sulfur) is abrupt at our site and meters below the soil-bedrock boundary, consistent with other fine-grained sedimentary bedrock weathering studies (Anderson, Dietrich, & Brimhall, 2002; Gu et al., 2020; Jin et al., 2010; Brantley, Holleran, et al., 2013, 2017; Winnick et al., 2017; Wan et al., 2019). Above the pyrite oxidation front, bedrock is extensively weathered. Across this front, color shifts from red hues to darker gray hues, which is consistent with a transition from oxidizing to reducing conditions. Some discrete fractures showing signs of iron oxidation persist beneath the pyrite oxidation front at our site. To delineate the pyrite oxidation front, we made the assumption that pyrite is the only sulfur-bearing mineral. While we are not aware of any other sulfur bearing minerals at our site, future work could characterize mineralogy via imaging and X-ray diffraction to confirm that pyrite is indeed the dominant or exclusive sulfur-bearing mineral.

The location of pyrite oxidation fronts has been linked to hillslope hydrologic dynamics and the lowest water table elevation (Chigira, 1990; Wan et al., 2019; Gu et al., 2020). However, pyrite has also been retained in matrix blocks within fractured, but otherwise poorly chemically weathered bedrock within the unsaturated zone (Anderson, Dietrich, & Brimhall, 2002). Across our study hillslopes, the water table is likely deeper than the pyrite oxidation front, because some neutron probe measurements in the unsaturated zone show moisture gains and losses beneath the oxidation front (Figure 6). Pyrite oxidation could be limited within the vadose zone if the bedrock matrix remains saturated or if reactive potential is exhausted at shallow depths within the vadose zone. Diffusive transport of oxygen to the interior of large, poorly fractured matrix blocks could occur slowly enough above the water table to limit oxidation. Fracture spacing in this case would play a role in the pace of oxidation (Reis & Brantley, 2017). Reactive transport modeling results indicate that under sufficiently low infiltration rates the water table can be deeper than the position of oxidative weathering fronts (Lebedeva & Brantley, 2020). Further work at the site is needed to evaluate the relationship between the water table elevation, reactive potential in the vadose zone, and the location of the pyrite oxidation front.

reaction fronts, with elements such as Mg, K, and Na showing coherent patterns of depletion (Figure 7). The depletion of Mg could be associated with chlorite dissolution, and the loss of K could be associated with illite dissolution as observed in Rose Hill shale (Brantley, Lebedeva, et al., 2017). However, a further mineralogical study is needed to link these elemental patterns to mineralogical transformations and their process controls. We observed depletion of both Fe and Al within the weathered bedrock, as also observed in Rose Hill shale at the Shale Hills CZO (Gu et al., 2020) and in contrast to the greywacke underlying Coos Bay, Oregon site (Anderson, Dietrich, & Brimhall, 2002), where Al and Fe depletion primarily occurred within the soil (we note, however, that samples are not reported between 1.5 and 3 m depth at that site due to lack of core recovery). If we assume the landscape has been in a state of steady erosion for long time periods, the cosmogenic-nuclide inferred erosion rate of  $\sim 0.072\text{--}0.131 \text{ mm yr}^{-1}$  results in a 100,000-years transit time of mineral grains through 7–13 m without vertical strain. Therefore, the chemical mass loss and porosity observed today likely took place under the inferred cooler and wetter climate regime of the Pleistocene.

There is likely a relationship between the initiation of chemical weathering, pervasive fracturing, and associated permeability generation. This correspondence between open and abundant fractures and chemical reaction fronts has been widely observed across a number of rock types, including sedimentary rocks (e.g., Anderson, Dietrich, & Brimhall, 2002; Gu et al., 2020; Wildman et al., 2004). At depths below Interface 3, both high and low angle fractures in otherwise unweathered bedrock are present and are typically closed without signs of iron oxidation. These deep, closed fractures probably do not play a major role in transmitting fluids that would propagate chemical weathering fronts (e.g., Anderson, Dietrich, & Brimhall, 2002). Because open and oxidized fractures that are both high and low angle are observed above both Interfaces 2 and 3, it is likely that the opening of these fractures initiates chemical weathering. Gu et al. (2020) hypothesize that the generation of microfractures that promote chemical weathering may depend on long-term erosion rates.

### 5.3. The Relationship Between Topography and Weathering

The thickness of weathering is the difference between the weathering front and the topographic surface. Here, we consider how these two surfaces may be related and how this relationship may vary with hillslope length. The relief of the topographic surface, as well as both Interfaces 2 and 3, scale with hillslope length (Figure 9), suggesting that the channel boundary condition at the base of the hillslope plays a role in the evolution of these three surfaces.

The diminishing downslope surface curvature on the study site ridges is consistent with hillslope erosion driven by non-linear soil transport (Roering et al., 2001). For a constant channel incision rate, the transport model predicts a linear relationship between hillslope length and topographic relief. Consistent with Roering et al. (2001), the mean slopes ( $Z_s/L$  in Table 1) are fairly consistent across hillslopes of different length, such that longer hillslopes have proportionally larger relief (Figure 9). Our preliminary cosmogenic-nuclide erosion rates suggest possible differences in erosion rate within the MH catchment, which would influence both ridge-valley spacing and mineral residence time. Variability in channel incision rate over short length-scales makes it more challenging to form direct comparisons of relief across hillslopes in the same catchment. For a mean incision rate of  $0.090 \text{ mm yr}^{-1}$  and weathered bedrock thickness at the ridgetop ranging from 7 to 18 m, residence time of the bedrock that arrives at the soil-bedrock interface could range from 69 to 194 kyr.

One mechanism by which the spatial pattern of weathering is related to topography could be through fracturing or fracture opening due to differential stresses associated with topography (Miller & Dunne, 1996). Topographically induced fractures are thought to occur in high curvature regions of the landscape, such as ridges and valleys (Savage & Swolfs, 1986; Slim et al., 2015). For example, topographically controlled jointing in channels may deepen oxidation fronts in Rose Hill shale (Brantley, Lebedeva, et al., 2017; Slim et al., 2015) and may lead to a feedback between channel incision, and physical and chemical weathering (Sullivan et al., 2016). At our site, valleys are locations of high curvature and channels are incising into relatively unweathered and unfractured bedrock. Deeper, more systematic drilling in valleys is needed to evaluate the extent to which the fractures intersected by our drilling are topographically controlled.

Some studies predict that opening-mode fracture patterns associated with topography result from the balance between stresses associated with regional compression and local topography (Moon et al., 2017; Slim et al., 2015). At our site, the regional stress has turned from an east-west dominated compression due to the subduction of the Farallon Plate to north-south compression since the transpressional tectonic system took place in this region in ~10 Ma (Atwater & Stock, 1998). At present, our study site has a relatively low-strain rate (<0.2  $\mu$ -strain/yr) based on GPS data (e.g., Murray et al., 2014). High regional compressive stresses are associated with open-mode fracture potential that mirror surface topography where the depth of weathering can extend beyond the hillslope relief, whereas low regional compressive stresses are associated with surface parallel fracture patterns that deepen upslope (Moon et al., 2017). While our observations are more consistent with a weathering profile predicted for low regional compressive stresses, more direct measurements of fracture density profile would be needed to evaluate these models. As there is no observation of offset along both high- and low-angle fractures, they are likely mode-I fractures (i.e., joints). Based on the strike and dip of the low-angle joints, they could be associated with the tilting of the originally horizontal Great Valley Sequence to the current bedding angle, which most likely occurred during the subduction of the Farallon Plate to the North American Plate (Atwater & Stock, 1998). Another possibility is that high angle jointing could result from bedrock exhumation and unloading. Given the complex tectonic history, it is an open question to what extent the contemporary stress field versus the multi-million-year tectonic legacy controls the generation and opening of fractures across the landscape.

Another possible mechanism connecting topography and weathering is the drainage of chemically equilibrated, stagnant pore fluid within unweathered bedrock. Rempe and Dietrich (2014) proposed that channel incision at the base of the hillslope couples the evolution of surface topography to the evolution of the weathering front. This is because channel incision drives both soil transport along the surface and the drainage of fluids from within the unweathered bedrock at depth. By considering steady state solutions to the coupled evolution of topography and bedrock drainage, Rempe and Dietrich (2014) predicted the combination of channel incision rate, hillslope dimensions, and soil and bedrock properties under which bedrock drainage may limit the depth of weathering. Rempe and Dietrich (2014) show that, for uniform channel incision rate and fresh bedrock properties (hydraulic conductivity and porosity), the mean slope of the weathering front should be constant across the landscape (i.e., the same under all hillslopes), and the weathering front relief increases with increasing hillslope length. This finding is consistent with our observations of both weathering fronts (Figure 9). Assuming steady state drainage of the unweathered bedrock is controlled by the pace of channel incision and the bedrock porosity, the hydraulic conductivity of the unweathered bedrock can be estimated from the mean slope of the weathering front. For the local mean incision rate of 0.09 mm/year and mean matrix porosity of 6.2% (Figure 6), the average inferred hydraulic conductivity calculated from Interface 2 and 3 across the three hillslopes is  $\sim 2 \times 10^{-10}$  m/s, which is reasonable for a fine-grained sedimentary bedrock (Freeze & Cherry, 1979; Gleeson et al., 2011).

While this hillslope drainage mechanism could reasonably explain the relationship between topography and weathering fronts we observe, this mechanism necessitates that the saturation state of the bedrock in the hillslope is determined by the hydraulic gradient set by the combination of the channel boundary condition, bedrock properties, and erosion rate. At our site, matrix blocks that retain pyrite may occur within the unsaturated zone, which is similar to what has been observed at a wetter site in Coos Bay Oregon (Anderson, Dietrich, & Brimhall, 2002). Such matrix blocks would be separated by unsaturated fractures and therefore disconnected from the hydraulic gradient set by the channel boundary conditions. Further work is needed to explore the controls on the desaturation or diffusive oxidation of these matrix blocks.

## 6. Conclusion

We document common patterns of subsurface bedrock weathering and water storage patterns across multiple individual unit hillslopes that make up a sequence of ridges and valleys with common tectonic history, lithology, and climate. Two sequential weathering fronts are identified: the shallower front is associated with pervasive fracturing and chemical alteration, while deeper chemical weathering is largely limited to discrete fractures and discoloration. Rainfall is seasonally stored as rock moisture within weathered bedrock (Figure 8) and likely an important source of moisture to the overlying plant community. The deep seasonal water storage in the weathered bedrock vadose zone has important consequences for water partitioning at

the site by sustaining summer dry season transpiration and mediating groundwater recharge. These findings can be used to investigate process coupling between bedrock weathering and landscape evolution, and further, provide a constraint for how individual hillslope measurements may be scaled up to watersheds comprised of an assemblage of hillslopes. Such scaling is needed to inform models of hillslope hydrology, slope stability, and earth system processes.

## Data Availability Statement

All data used in the publication are cited in the references and hosted on Consortium of Universities for the Advancement of Hydrologic Science, Inc. (CUAHSI)'s web based hydrologic information system (<https://doi.org/10.4211/hs.d49c5e4539a64d8f8e26e7f2668bdeb3>).

## Acknowledgments

Funding sources for this project include the US Department of Energy, Office of Science, Office of Biological Environmental Research under award number DESC0018039, the National Science Foundation supported Eel River Critical Zone Observatory (NSF EAR 1331940), the Carol Baird Graduate Student Award for Field Research, University of California Institute for the Study of Ecological Effects of Climate Impacts, the University of California Berkeley Charles H. Ramsden Endowed Scholarship Fund, and the Jackson School of Geosciences. The authors thank Jerry Brown, Anne Gust Brown, Rhonda Gruber and Greg Hemmi for generous land access and scientific enthusiasm; Maryn Sanders, Logan Schmidt, Emma Sevier, Micaela Pedrazas, Chloe Fisher, and Brandon Minton for support in the lab and field; and Joel Johnson for his thoughtful revision of the manuscript. The authors also thank Kuni Nishizumi and Kees Welton for generously sharing their laboratory and expertise with respect to cosmogenic-nuclide sample processing; Behnaz Hosseini and Anna Mikheicheva for their assistance with quartz separation; and Marissa Tremblay for insight regarding erosion-rate calculations.

## References

- Adam, D. P., Sims, J. D., & Throckmorton, C. K. (1981). 130,000-yr continuous pollen record from Clear Lake, Lake County, California. *Geology*, 9(8), 373–377. [https://doi.org/10.1130/0091-7613\(1981\)9\(373:YCPRFC\)2.0.CO;2](https://doi.org/10.1130/0091-7613(1981)9(373:YCPRFC)2.0.CO;2)
- Adam, D. P., & West, G. J. (1983). Temperature and Precipitation Estimates Through the Last Glacial Cycle from Clear Lake, California, Pollen Data. *Science*, 219(4581), 168–170. <https://doi.org/10.1126/science.219.4581.168>
- Anderson, R. S., Anderson, S. P., & Tucker, G. E. (2013). Rock damage and regolith transport by frost: An example of climate modulation of the geomorphology of the critical zone. *Earth Surface Processes and Landforms*, 38(3), 299–316. <https://doi.org/10.1002/esp.3330>
- Anderson, R. S., Rajaram, H., & Anderson, S. P. (2019). Climate driven coevolution of weathering profiles and hillslope topography generates dramatic differences in critical zone architecture. *Hydrological Processes*, 33(1), 4–19.
- Anderson, S. P., Dietrich, W. E., & Brimhall, G. H., Jr. (2002). Weathering profiles, mass-balance analysis, and rates of solute loss: Linkages between weathering and erosion in a small, steep catchment. *The Geological Society of America Bulletin*, 116.
- Arkley, R. J. (1981). Soil moisture use by mixed conifer forest in a summer-dry climate 1. *Soil Science Society of America Journal*, 45(2), 423. <https://doi.org/10.2136/sssaj1981.03615995004500020037x>
- Armstrong, A. C. (1980). Simulated slope development sequences in a three-dimensional context. *Earth Surface Processes*, 5(3), 265–270. <https://doi.org/10.1002/esp.3760050304>
- Atwater, T., & Stock, J. (1998). Pacific-north america plate tectonics of the neogene southwestern united states: an update. *International Geology Review*, 40(5), 375–402.
- Balco, G., Stone, J. O., Lifton, N. A., & Dunai, T. J. (2008). A complete and easily accessible means of calculating surface exposure ages or erosion rates from  $^{10}\text{Be}$  and  $^{26}\text{Al}$  measurements. *Quaternary Geochronology*, 3(3), 174–195. <https://doi.org/10.1016/j.quageo.2007.12.001>
- Bartolome, J. W., Klukkert, S. E., & Barry, W. J. (1986). Opal Phytoliths as Evidence for Displacement of Native Californian Grassland. *Madroño*, 33(3), 217–222.
- Bennett, G. L., Roering, J. J., Mackey, B. H., Handwerger, A. L., Schmidt, D. A., & Guillod, B. P. (2016). Historic drought puts the brakes on earthflows in Northern California: Drought Puts Breaks on Earthflows. *Geophysical Research Letters*, 43(11), 5725–5731. <https://doi.org/10.1002/2016GL068378>
- Booth, A. M., Roering, J. J., & Rempel, A. W. (2013). Topographic signatures and a general transport law for deep-seated landslides in a landscape evolution model. *Journal of Geophysical Research: Earth Surface*, 118(2), 603–624. <https://doi.org/10.1002/jgrf.20051>
- Brantley, S. L., Holleran, M. E., Jin, L., & Bazilevskaya, E. (2013). Probing deep weathering in the Shale Hills Critical Zone Observatory, Pennsylvania (USA): The hypothesis of nested chemical reaction fronts in the subsurface. *Earth Surface Processes and Landforms*, 38(11), 1280–1298. <https://doi.org/10.1002/esp.3415>
- Brantley, S. L., & Lebedeva, M. (2011). Learning to Read the Chemistry of Regolith to Understand the Critical Zone. *Annual Review of Earth and Planetary Sciences*, 39(1), 387–416. <https://doi.org/10.1146/annurev-earth-040809-152321>
- Brantley, S. L., Lebedeva, M. I., Balashov, V. N., Singha, K., Sullivan, P. L., & Stinchcomb, G. (2017). Toward a conceptual model relating chemical reaction fronts to water flow paths in hills. *Geomorphology*, 277, 100–117. <https://doi.org/10.1016/j.geomorph.2016.09.027>
- Brimhall, G. H., & Dietrich, W. E. (1987). Constitutive mass balance relations between chemical composition, volume, density, porosity, and strain in metasomatic hydrochemical systems: Results on weathering and pedogenesis. *Geochimica et Cosmochimica Acta*, 51(3), 567–587. [https://doi.org/10.1016/0016-7037\(87\)90070-6](https://doi.org/10.1016/0016-7037(87)90070-6)
- Burcham, L. (1970). *Ecological significance of alien plants in California grasslands*. Proceedings of the association of American Geographers (Vol. 2, p. 36–39).
- Canadell, J., Jackson, R. B., Ehleringer, J. R., Mooney, H. A., Sala, O. E., & Schulze, E.-D. (1996). Maximum rooting depth of vegetation types at the global scale. *Oecologia*, 108(4), 583–595. <https://doi.org/10.1007/BF00329030>
- Chigira, M. (1990). A mechanism of chemical weathering of mudstone in a mountainous area. *Engineering Geology*, 29(2), 119–138. [https://doi.org/10.1016/0013-7952\(90\)90002-I](https://doi.org/10.1016/0013-7952(90)90002-I)
- Constenius, K. N., Johnson, R. A., Dickinson, W. R., & Williams, T. A. (2000). Tectonic evolution of the Jurassic-Cretaceous Great Valley forearc, California: Implications for the Franciscan thrust-wedge hypothesis. *GSA Bulletin*, 112(11), 1703–1723. [https://doi.org/10.1130/0016-7606\(2000\)112\(1703:TEOTJC\)2.0.CO;2](https://doi.org/10.1130/0016-7606(2000)112(1703:TEOTJC)2.0.CO;2)
- DiBiase, R. A. (2018). Short communication: Increasing vertical attenuation length of cosmogenic nuclide production on steep slopes negates topographic shielding corrections for catchment erosion rates. *Earth Surface Dynamics*, 6(4), 923–931. <https://doi.org/10.5194/esurf-6-923-2018>
- Dietrich, W. (2019). *High resolution mapping of antelope valley ranch, ca*. National Center for Airborne Laser Mapping (NCALM). <https://doi.org/10.5069/G9QC01MQ>
- Dohrenwend, J. (1974). *Geology of the central Salinas valley and adjacent uplands, Monterey county, California (Unpublished doctoral dissertation)*. Ph.D. thesis. Stanford University.
- Ernst, W. G. (1970). Tectonic contact between the Franciscan Mélange and the Great Valley Sequence—Crustal expression of a Late Mesozoic Benioff Zone. *Journal of Geophysical Research*, 75(5), 886–901. <https://doi.org/10.1029/JB075i005p00886>

- Fan, Y., Clark, M., Lawrence, D. M., Swenson, S., Band, L., Brantley, S. L., & others (2019). Hillslope hydrology in global change research and Earth system modeling. *Water Resources Research*, 55(2), 1737–1772.
- France-Lanord, C., & Derry, L. A. (1997). Organic carbon burial forcing of the carbon cycle from Himalayan erosion. *Nature*, 390(6655), 65–67. <https://doi.org/10.1038/36324>
- Freeze, R. A., & Cherry, J. A. (1979). *Groundwater (Tech. Rep.)*.
- Gilbert, G. K. (1909). The convexity of hilltops. *The Journal of Geology*, 17(4), 344–350.
- Gleeson, T., Smith, L., Moosdorf, N., Hartmann, J., Dürr, H. H., Manning, A. H., & Jellinek, A. M. (2011). Mapping permeability over the surface of the Earth. *Geophysical Research Letters*, 38(2). <https://doi.org/10.1029/2010GL045565>
- Goodfellow, B. W., Hilley, G. E., & Schulz, M. S. (2011). Vadose zone controls on weathering intensity and depth: Observations from grusitic saprolites. *Applied Geochemistry*, 26, S36-S39. <https://doi.org/10.1016/j.apgeochem.2011.03.023>
- Gu, X., Rempe, D. M., Dietrich, W. E., West, A. J., Lin, T.-C., Jin, L., & Brantley, S. L. (2020). Chemical reactions, porosity, and microfracturing in shale during weathering: The effect of erosion rate. *Geochimica et Cosmochimica Acta*, 269, 63–100. <https://doi.org/10.1016/j.gca.2019.09.044>
- Hack, J. T., & Goodlett, J. C. (1960). *Geomorphology and forest ecology of a mountain region in the central appalachians (Tech. Rep.)*. United States Government Printing Office.
- Hackel, O. (1966). Summary of the geology of the great valley. *Geology of Northern California. Bulletin*, 190, 217–238.
- Hahm, W. J., Rempe, D. M., Dralle, D. N., Dawson, T. E., Lovill, S. M., Bryk, A. B., & Dietrich, W. E. (2019). Lithologically controlled subsurface critical zone thickness and water storage capacity determine regional plant community composition. *Water Resources Research*, 55(4), 3028–3055. <https://doi.org/10.1029/2018WR023760>
- Harman, C. J., & Cosans, C. L. (2019). A low-dimensional model of bedrock weathering and lateral flow coevolution in hillslopes: 2. Controls on weathering and permeability profiles, drainage hydraulics, and solute export pathways. *Hydrological Processes*, 33(8), 1168–1190. <https://doi.org/10.1002/hyp.13385>
- Hasenmueller, E. A., Gu, X., Weitzman, J. N., Adams, T. S., Stinchcomb, G. E., Eissenstat, D. M., & Kaye, J. P. (2017). Weathering of rock to regolith: The activity of deep roots in bedrock fractures. *Geoderma*, 300, 11–31. <https://doi.org/10.1016/j.geoderma.2017.03.020>
- Heimsath, A. M., Dietrich, W. E., Nishiizumi, K., & Finkel, R. C. (1997). The soil production function and landscape equilibrium. *Nature*, 388(6640), 358–361. <https://doi.org/10.1038/41056>
- Hilley, G., Chamberlain, C., Moon, S., Porder, S., & Willett, S. (2010). Competition between erosion and reaction kinetics in controlling silicate-weathering rates. *Earth and Planetary Science Letters*, 293(1), 191–199. <https://doi.org/10.1016/j.epsl.2010.01.008>
- Hirano, M. (1975). Simulation of developmental process of interfluvial slopes with reference to graded form. *The Journal of Geology*, 83(1), 113–123. <https://doi.org/10.1086/628048>
- Holbrook, W. S., Marcon, V., Bacon, A. R., Brantley, S. L., Carr, B. J., Flinchum, B. A., & Riebe, C. S. (2019). Links between physical and chemical weathering inferred from a 65-m-deep borehole through Earth's critical zone. *Scientific Reports*, 9(1), 4495. <https://doi.org/10.1038/s41598-019-40819-9>
- Hovius, N. (1996). Regular spacing of drainage outlets from linear mountain belts. *Basin Research*, 8(1), 29–44. <https://doi.org/10.1111/j.1365-2117.1996.tb00113.x>
- Hubbert, K., Beyers, J., & Graham, R. (2001). Roles of weathered bedrock and soil in seasonal water relations of *Pinus Jeffreyi* and *Arctostaphylos patula*. *Canadian Journal of Forest Research*, 31(11), 1947–1957. <https://doi.org/10.1139/cjfr-31-11-1947>
- Jackson, R. B., Moore, L. A., Hoffmann, W. A., Pockman, W. T., & Linder, C. R. (1999). Ecosystem rooting depth determined with caves and DNA. *Proceedings of the National Academy of Sciences*, 96, 11387–11392. <https://doi.org/10.1073/pnas.96.20.11387>
- Jin, L., Ravella, R., Ketchum, B., Bierman, P. R., Heaney, P., White, T., & Brantley, S. L. (2010). Mineral weathering and elemental transport during hillslope evolution at the Susquehanna/Shale Hills Critical Zone Observatory. *Geochimica et Cosmochimica Acta*, 74(13), 3669–3691. <https://doi.org/10.1016/j.gca.2010.03.036>
- Kohl, C. P., & Nishiizumi, K. (1992). Chemical isolation of quartz for measurement of in-situ-produced cosmogenic nuclides. *Geochimica et Cosmochimica Acta*, 56(9), 3583–3587. [https://doi.org/10.1016/0016-7037\(92\)90401-4](https://doi.org/10.1016/0016-7037(92)90401-4)
- Lebedeva, M., & Brantley, S. (2020). Relating the depth of the water table to depth of weathering. *Earth Surface Processes and Landforms*. <https://doi.org/10.1002/esp.4873>
- Lewis, D. C., & Burgi, R. H. (1964). The Relationship between oak tree roots and groundwater in fractured rock as determined by tritium tracing. *Journal of Geophysical Research*, 69(12), 2579–2588. <https://doi.org/10.1029/JZ069i012p02579>
- Lifton, N., Sato, T., & Dunai, T. J. (2014). Scaling in situ cosmogenic nuclide production rates using analytical approximations to atmospheric cosmic-ray fluxes. *Earth and Planetary Science Letters*, 386, 149–160. <https://doi.org/10.1016/j.epsl.2013.10.052>
- Long, I. F., & French, B. K. (1967). Measurement of Soil Moisture in the Field by Neutron Moderation. *Journal of Soil Science*, 18(1), 149–166. <https://doi.org/10.1111/j.1365-2389.1967.tb01496.x>
- Lovill, S. M., Hahm, W. J., & Dietrich, W. E. (2018). Drainage from the Critical Zone: Lithologic Controls on the Persistence and Spatial Extent of Wetted Channels during the Summer Dry Season. *Water Resources Research*, 54(8), 5702–5726. <https://doi.org/10.1029/2017WR021903>
- Micromeritics. (2019a). *AccuPyc II 1340 pycnometer*. Retrieved from <https://www.micromeritics.com/Product-Showcase/AccuPyc-II-1340.aspx>
- Micromeritics. (2019b). *GeoPyc 1365 envelope density analyzer*. Retrieved from <https://www.micromeritics.com/Product-Showcase/GeoPyc-1360-Envelope-Density-Analyzer.aspx>
- Miller, D. J., & Dunne, T. (1996). Topographic perturbations of regional stresses and consequent bedrock fracturing. *Journal of Geophysical Research*, 101(B11), 25523–25536. <https://doi.org/10.1029/96JB02531>
- Montgomery, D. R., & Dietrich, W. E. (1994). A physically based model for the topographic control on shallow landsliding. *Water Resources Research*, 30(4), 1153–1171.
- Montgomery, D. R., Dietrich, W. E., Torres, R., Anderson, S. P., Heffner, J. T., & Loague, K. (1997). Hydrologic response of a steep, unchanneled valley to natural and applied rainfall. *Water Resources Research*, 33(1), 91–109.
- Moon, S., Perron, J. T., Martel, S. J., Holbrook, W. S., & St Clair, J. (2017). A model of three-dimensional topographic stresses with implications for bedrock fractures, surface processes, and landscape evolution. *Journal of Geophysical Research: Earth Surface*, 122(4), 823–846. <https://doi.org/10.1002/2016JF004155>
- Murray, J. R., Minson, S. E., & Svart, J. L. (2014). Slip rates and spatially variable creep on faults of the northern San Andreas system inferred through Bayesian inversion of global positioning system data. *Journal of Geophysical Research: Solid Earth*, 119(7), 6023–6047.
- Nelson, M. D., Bryk, A. B., Fauria, K., Huang, M. H., & Dietrich, W. E. (2017). Physical properties of shallow landslides and their role in landscape evolution investigated with ultrahigh-resolution lidar data and aerial imagery. AGU fall meeting Abstracts.

- Nesbitt, H. W. (1979). Mobility and fractionation of rare earth elements during weathering of a granodiorite. *Nature*. <https://doi.org/10.1038/279206a0>
- Nie, Y.-P., Chen, H.-S., Wang, K.-L., Tan, W., Deng, P.-Y., & Yang, J. (2011). Seasonal water use patterns of woody species growing on the continuous dolostone outcrops and nearby thin soils in subtropical China. *Plant and Soil*, 341(1–2), 399–412. <https://doi.org/10.1007/s11104-010-0653-2>
- O'Callaghan, J. F., & Mark, D. M. (1984). The extraction of drainage networks from digital elevation data. *Computer Vision, Graphics, and Image Processing*, 28(3), 323–344.
- Onda, Y., Komatsu, Y., Tsujimura, M., & Fujihara, J.-i. (2001). The role of subsurface runoff through bedrock on storm flow generation. *Hydrological Processes*, 15(10), 1693–1706. <https://doi.org/10.1002/hyp.234>
- Onda, Y., Tsujimura, M., & Tabuchi, H. (2004). The role of subsurface water flow paths on hillslope hydrological processes, landslides and landform development in steep mountains of Japan. *Hydrological Processes*, 18(4), 637–650. <https://doi.org/10.1002/hyp.1362>
- Pelletier, J. D., Broxton, P. D., Hazenberg, P., Zeng, X., Troch, P. A., Niu, G.-Y., & Gochis, D. (2016). A gridded global data set of soil, intact regolith, and sedimentary deposit thicknesses for regional and global land surface modeling. *Journal of Advances in Modeling Earth Systems*, 8(1), 41–65.
- Perron, J. T., Dietrich, W. E., & Kirchner, J. W. (2008). Controls on the spacing of first-order valleys. *Journal of Geophysical Research*, 113(F4), F04016. <https://doi.org/10.1029/2007JF000977>
- Perron, J. T., Kirchner, J. W., & Dietrich, W. E. (2009). Formation of evenly spaced ridges and valleys. *Nature*, 460(7254), 502–505. <https://doi.org/10.1038/nature08174>
- PRISM Climate Group. (2020). PRISM rainfall dataset. PRISM Climate Group.
- Reis, F. D. A., & Brantley, S. L. (2017). Models of transport and reaction describing weathering of fractured rock with mobile and immobile water. *Journal of Geophysical Research: Earth Surface*, 122(3), 735–757.
- Rempe, D. M., & Dietrich, W. E. (2014). A bottom-up control on fresh-bedrock topography under landscapes. *Proceedings of the National Academy of Sciences*, 111, 6576–6581. <https://doi.org/10.1073/pnas.1404763111>
- Rempe, D. M., & Dietrich, W. E. (2018). Direct observations of rock moisture, a hidden component of the hydrologic cycle. *Proceedings of the National Academy of Sciences*, 115, 2664–2669. <https://doi.org/10.1073/pnas.1800141115>
- Rich, E. I. (1971). *Geologic map of the wilbur springs quadrangle, Colusa and lake counties, California* (Tech. Rep.).
- Riebe, C. S., & Granger, D. E. (2013). Quantifying effects of deep and near-surface chemical erosion on cosmogenic nuclides in soils, saprolite, and sediment. *Earth Surface Processes and Landforms*, 38(5), 523–533. <https://doi.org/10.1002/esp.3339>
- Riebe, C. S., Hahm, W. J., & Brantley, S. L. (2017). Controls on deep critical zone architecture: A historical review and four testable hypotheses: Four testable hypotheses about the Deep Critical Zone. *Earth Surface Processes and Landforms*, 42(1), 128–156. <https://doi.org/10.1002/esp.4052>
- Roering, J. J., Kirchner, J. W., & Dietrich, W. E. (2001). Hillslope evolution by nonlinear, slope-dependent transport: Steady state morphology and equilibrium adjustment timescales. *Journal of Geophysical Research*, 106(B8), 16499–16513. <https://doi.org/10.1029/2001JB000323>
- Rose, K., Graham, R., & Parker, D. (2003). Water source utilization by Pinus jeffreyi and *Arctostaphylos patula* on thin soils over bedrock. *Oecologia*, 134(1), 46–54. <https://doi.org/10.1007/s00442-002-1084-4>
- Ruxton, V. B. P., & Berry, L. (1959). *The basal rock surface on weathered granitic rocks*. Proceedings of the Geologists' association. [https://doi.org/10.1016/S0016-7878\(59\)80010-9](https://doi.org/10.1016/S0016-7878(59)80010-9)
- Ryu, Y., Baldocchi, D. D., Kobayashi, H., van Ingen, C., Li, J., Black, T. A., & Roupsard, O. (2011). Integration of MODIS land and atmosphere products with a coupled-process model to estimate gross primary productivity and evapotranspiration from 1 km to global scales. *Global Biogeochemical Cycles*, 25(4). <https://doi.org/10.1029/2011GB004053>
- Salve, R., Rempe, D. M., & Dietrich, W. E. (2012). Rain, rock moisture dynamics, and the rapid response of perched groundwater in weathered, fractured argillite underlying a steep hillslope. *Water Resources Research*, 48(11). <https://doi.org/10.1029/2012WR012583>
- Sanders, M., Nelson, M. D., Bryk, A. B., Huang, M.-H., Fauria, K., & Dietrich, W. E. (2019). The role of small shallow landslides in landscape evolution as revealed by high resolution differential lidar surveys and field mapping. In *AGU fall meeting 2019*. AGU.
- Savage, W. Z., & Swolfs, H. S. (1986). Tectonic and gravitational stress in long symmetric ridges and valleys. *Journal of Geophysical Research*, 91(B3), 3677–3685.
- Schoeneberger, P. J., Amoozegar, A., & Buol, S. W. (1995). Physical Property Variation of a Soil and Saprolite Continuum at Three Geomorphic Positions. *Soil Science Society of America Journal*, 59(5), 1389–1397. <https://doi.org/10.2136/sssaj1995.03615995005900050027x>
- Scholl, D. G. (1976). Soil Moisture Flux and Evapotranspiration Determined from Soil Hydraulic Properties in a Chaparral Stand. *Soil Science Society of America Journal*, 40(1), 14. <https://doi.org/10.2136/sssaj1976.03615995004000010009x>
- Schwinning, S. (2010). The ecohydrology of roots in rocks. *Ecohydrology*, 3(2), 238–245. <https://doi.org/10.1002/eco.134>
- Serra, O. (1989). *Formation MicroScanner image interpretation*. Schlumberger Educational Services.
- Shaler, N. S. (1899). Spacing of rivers with reference to hypothesis of baseleveling. *The Geological Society of America Bulletin*, 10(1), 263–276. <https://doi.org/10.1130/GSAB-10-263>
- Sklar, L. S., Riebe, C. S., Marshall, J. A., Genetti, J., Leclere, S., Lukens, C. L., & Merces, V. (2017). The problem of predicting the size distribution of sediment supplied by hillslopes to rivers. *Geomorphology*, 277, 31–49. <https://doi.org/10.1016/j.geomorph.2016.05.005>
- Slim, M., Perron, J. T., Martel, S. J., & Singha, K. (2015). Topographic stress and rock fracture: A two-dimensional numerical model for arbitrary topography and preliminary comparison with borehole observations. *Earth Surface Processes and Landforms*, 40(4), 512–529. <https://doi.org/10.1002/esp.3646>
- St Clair, J., Moon, S., Holbrook, W. S., Perron, J. T., Riebe, C. S., Martel, S. J., & d. Richter, D. (2015). Geophysical imaging reveals topographic stress control of bedrock weathering. *Science*, 350(6260), 534–538. <https://doi.org/10.1126/science.aab2210>
- Sternberg, P., Anderson, M., Graham, R., Beyers, J., & Tice, K. (1996). Root distribution and seasonal water status in weathered granitic bedrock under chaparral. *Geoderma*, 72(1–2), 89–98. [https://doi.org/10.1016/0016-7061\(96\)00019-5](https://doi.org/10.1016/0016-7061(96)00019-5)
- Sullivan, P., Hynek, S., Gu, X., Singha, K., White, T., West, N., & Brantley, S. (2016). Oxidative dissolution under the channel leads geomorphological evolution at the Shale Hills catchment. *American Journal of Science*, 316(10), 981–1026.
- Talling, P. J., Stewart, M. D., Stark, C. P., Gupta, S., & Vincent, S. J. (1997). Regular spacing of drainage outlets from linear fault blocks. *Basin Research*, 9(4), 275–302. <https://doi.org/10.1046/j.1365-2117.1997.00048.x>
- Uchida, T., Kosugi, K., & Mizuyama, T. (2002). Effects of pipe flow and bedrock groundwater on runoff generation in a steep headwater catchment in Ashiu, central Japan: Pipe flow and bedrock groundwater effects on runoff. *Water Resources Research*, 38(7), 241–244. <https://doi.org/10.1029/2001WR000261>
- Unruh, J. R., & Moores, E. M. (1992). Quaternary blind thrusting in the southwestern Sacramento Valley, California. *Tectonics*, 11(2), 192–203. <https://doi.org/10.1029/91TC02494>

- Wan, J., Tokunaga, T. K., Williams, K. H., Dong, W., Brown, W., Henderson, A. N., & Hubbard, S. S. (2019). Predicting sedimentary bedrock subsurface weathering fronts and weathering rates. *Scientific Reports*, 9(1), 1–10. <https://doi.org/10.1038/s41598-019-53205-2>
- Wildman, R., Berner, R., Petsch, S., Bolton, E., Eckert, J., Mok, U., & Evans, J. (2004). The weathering of sedimentary organic matter as a control on atmospheric O<sub>2</sub>: I. Analysis of a black shale. *American Journal of Science*, 304(3), 234–249.
- Willett, S. D., Slingerland, R., & Hovius, N. (2001). Uplift, shortening, and steady state topography in active mountain belts. *American Journal of Science*, 301(4–5), 455–485.
- Winnick, M. J., Carroll, R. W. H., Williams, K. H., Maxwell, R. M., Dong, W., & Maher, K. (2017). Snowmelt controls on concentration-discharge relationships and the balance of oxidative and acid-base weathering fluxes in an alpine catchment, East River, Colorado. *Water Resources Research*, 53(3), 2507–2523. <https://doi.org/10.1002/2016WR019724>
- Witty, J. H., Graham, R. C., Hubbert, K. R., Doolittle, J. A., & Wald, J. A. (2003). Contributions of water supply from the weathered bedrock zone to forest soil quality. *Geoderma*, 114(3–4), 389–400. [https://doi.org/10.1016/S0016-7061\(03\)00051-X](https://doi.org/10.1016/S0016-7061(03)00051-X)
- Zwieniecki, M. A., & Newton, M. (1996). Seasonal pattern of water depletion from soil–rock profiles in a Mediterranean climate in southwestern Oregon. *Canadian Journal of Forest Research*, 26(88), 1346–1352.